International Journal of Impact Engineering 144 (2020) 103655

Contents lists available at ScienceDirect

International Journal of Impact Engineering

journal homepage: www.elsevier.com/locate/ijimpeng

Experimental verification of a crystal plasticity-based simulation framework for predicting microstructure and geometric shape changes: Application to bending and Taylor impact testing of Zr

Evgenii Vasilev[a], Miroslav Zecevic[b], Rodney J. McCabe[c], Marko Knezevic[a,*]

[a] Department of Mechanical Engineering, University of New Hampshire, Durham, NH 03824, USA
[b] Theoretical Division, Los Alamos National Laboratory, Los Alamos, NM 87545, USA
[c] Materials Science and Technology Division, Los Alamos National Laboratory, Los Alamos, NM 87545, USA

ARTICLE INFO

Keywords:
Microstructures
Twinning
Crystal plasticity
Impact testing
Finite elements
Zirconium

ABSTRACT

This paper is concerned with experimental verification of a recently developed multi-scale simulation framework for plastic deformation of metallic materials from quasi-static to impact deformation conditions. The framework is a visco-plastic self-consistent (VPSC) polycrystalline model embedded in an implicit finite element method (FE-VPSC) to provide a microstructure-sensitive constitutive response at each material point. Each material point of the FEM model is a polycrystalline aggregate with crystallographic deformation mechanisms operating at the single crystal scale with their evolving activity based on a dislocation density-based hardening law and texture. Four beams and three cylinders machined in different orientations from a textured plate of high-purity zirconium are tested quasi-statically in 4-point bending and at speeds of 100 m/s, 170 m/s and 243 m/s during Taylor impact tests, respectively. The variation in dimensional changes resulting from different sample orientations in the plate with respect to loading directions is measured for each sample. Moreover, texture and twinning characterization is performed using electron backscattered diffraction (EBSD). The deformation processes and underlying evolution of microstructure are successfully simulated using the FE-VPSC framework. In doing so, the model parameters are optimized and validated across a broad range of strain rates and temperatures. Simulation results in terms of geometrical changes and microstructural evolution are compared with the experimental measurements. The model predicts anisotropic material flow resulting from the hard-to-deform crystallographic directions, the development of gradients in texture and twinning through the geometries, tension–compression asymmetry, as well as the extent of plasticity under impact.

1. Introduction

Alloys of zirconium (Zr) are important for a number of practical applications in the nuclear industry, primarily due to their low absorption of neutrons as well as good corrosion resistance [1, 2]. High purity Zr is used for fundamental understanding of the material behavior. The deformation behavior of Zr is highly anisotropic and sensitive to changes in temperature and strain-rate conditions [3]. Such behavior is a consequence of its hexagonal close packed (HCP) crystal structure governed by the activation of multiple slip and twinning modes. Activation of a deformation system/mode requires overcoming the critical resolved shear stress (CRSS) of the system/mode. The activation depends on temperature and strain-rate. The CRSS evolves with plastic strain as the temperature and strain rate dependent dislocation density evolves. As a result, predicting deformation behavior during shaping and forming or in service requires knowledge of the crystallography, i.e. slip/twinning and texture.

This work is concerned with mechanical behavior and microstructural evolution of high-purity Zr deforming plastically over a broad range of strain rates at two temperatures (room and liquid nitrogen). Several dynamic tests exist for testing material behavior across a range of strain-rates. These tests include split Hopkinson pressure bar, Taylor cylinder impact, flyer plate impact, and laser shock [4-9]. The first two reach strain rates in the range of 10^2 /s - 10^5 /s, whereas the latter two can attain strain-rates in excess of 10^6 /s. The split Hopkinson pressure bar test allows for high strain-rate stress/strain curves to be obtained and tested samples can be analyzed post-mortem. However, a stress-strain curve cannot be obtained using the other three tests that only

* Corresponding Author. University of New Hampshire, Department of Mechanical Engineering, 33 Academic Way, Kingsbury Hall, W119, Durham, New Hampshire 03824, United States
E-mail address: marko.knezevic@unh.edu (M. Knezevic).

https://doi.org/10.1016/j.ijimpeng.2020.103655
Received 15 May 2020; Accepted 21 June 2020
Available online 23 June 2020
0734-743X/

provide samples for post-mortem analysis. The Taylor impact test was originally developed as a way to determine dynamic yielding of polycrystalline metals by propelling a cylindrical specimen at a rigid target [10]. The tested material experiences a wide range of strain-rates and strain levels, and a single sample can be used to validate constitutive laws for a range of strain-rates and strains [11-13]. Metals of varying crystal structures have been tested, such as Ta, Ti, and Zr [14-17], allowing the development and validation of crystal plasticity models [18-26]. To this end, the cross-sectional shape changes along the length of a cylinder are measured. Moreover, the underlying microstructural evolution can be characterized. As a result of the highly heterogeneous deformation imposed by this test, substantial variations in microstructure are usually observed throughout a cylinder [17].

Material models are often fit using stress-strain data at a range of strain-rates and/or temperatures measured using quasi-static mechanical tests and split Hopkinson pressure bar tests. The predictive characteristics of the models can then be extrapolated/evaluated by simulating Taylor impact tests. For Taylor impact simulations of Ta, a finite element (FE) model with constitutive laws based on continuum yield surfaces was found to be sufficient for modeling the shape changes during the test. The good predictions were associated with the high symmetry body center-cubic (BCC) structure of Ta governing the relatively isotropic material flow [14]. However, similar modeling approaches were not sufficient for materials with a lower symmetry HCP structure such as Zr [11]. The evolution of texture and the specific deformation mechanisms underlying plastic deformation, including deformation twinning, need to be incorporated in the models. The importance of considering these effects in a Taylor impact test was recently discussed in a study on Ti, another HCP metal [27]. The work predicted the geometric changes during the test by developing a specialized anisotropic yield surface that approximates the tension-compression asymmetry and effects of texture and twinning [27]. Such specialized continuum models rely on fitting of macroscopic data and do not consider the deformation physics of crystallographic slip and twinning. In contrast, crystal plasticity models take into account the physics of deformation more explicitly. For several decades, such models have been pursued to describe the behavior of metals by considering the microstructural features and the crystallography of deformation mechanisms. In these models, the strain-rate dependence in the material response arises from stress driven activation of the fundamental deformation mechanisms that depend on the microstructural evolution. As a result, these models improve predictive characteristics of anisotropic material flow as well as facilitate better understanding of the deformation behavior of polycrystals.

This work utilizes a recent finite element implementation of the visco-plastic self-consistent (FE-VPSC) model to simulate the evolution of texture, twinning, and geometry of high-purity Zr during compression, bending, and Taylor impact tests. Four beams and three cylinders were machined from a textured plate of Zr along different directions and quasi-statically tested in 4-point bending and in Taylor impact at speeds of 100 m/s, 170 m/s and 243 m/s, respectively. We acknowledge that the bending experiments were presented in an earlier work [28]. The variation in dimensional changes resulting from different sample orientations in the plate with respect to loading directions was measured for each sample. The deformed geometry and texture evolution per beam were used in the present work to evaluate predictive characteristics of the modeling framework under quasi-static strain rates. Likewise, deformed geometry, texture, and twinning characterization was performed using electron backscattered diffraction (EBSD) for the impacted cylinders to facilitate model evaluation under impact deformation. The deformation processes of compression, bending, and impact along with the underlying evolution of microstructure were successfully simulated using the FE-VPSC model. The predictive characteristics of the model were evaluated from quasi-static to high strain-rate to impact deformation conditions. In doing so, the model parameters are optimized and validated across a broad range of strain rates and temperatures. It is shown that the predictions and measurements of texture, twin volume fraction, and geometry are in good agreement. Although the model is primarily calibrated and validated using stress-strain curves and microstructural data up to the strain-rates achieved in the testing by Split-Hopkinson pressure bar, the extrapolated predictions to much higher strain rates achieve good agreement with minimal further adjustments of the material parameters. Hence, the thermally activated dislocation density-based hardening model is valid at much higher strain-rate fields induced by the impacts varying heterogeneously both spatially and temporarily. As a result, the dislocation glide is likely to be thermally-activated even at the strain-rates in the Taylor impact tests.

2. Modelling framework

The homogenized response of a polycrystalline aggregate can be efficiently calculated using the VPSC model. In VPSC, the polycrystalline aggregate is represented by a set of single crystalline ellipsoidal grains, each described by the shape and orientation of the ellipsoid, orientation of the crystal lattice inside the ellipsoid, and volume fraction. Each grain deforms by crystallographic slip and twinning. Twinning is treated as pseudo-slip followed by a crystal lattice reorientation of the twinned domain upon a critical amount of its activity/fraction. The slip shear rate is given by the power-law relationship [29,30]:

$$\dot{\gamma}^{s(r)} = \dot{\gamma}_0 \left(\frac{|\boldsymbol{\sigma}'^{(r)} \cdot \mathbf{m}^{s(r)}|}{\tau_c^{s(r)}} \right)^n sign(\boldsymbol{\sigma}'^{(r)} \cdot \mathbf{m}^{s(r)}) , \tag{1}$$

where $\dot{\gamma}^{s(r)}$ is the shear rate on system s in grain r, $\boldsymbol{\sigma}'^{(r)}$ is the Cauchy deviatoric stress in grain r, $\tau_c^{s(r)}$ is the slip resistance, $\dot{\gamma}_0$ is the reference shear rate taken as unity, n is the power-law exponent (inverse of rate sensitivity), and $\mathbf{m}^{s(r)}$ is the symmetric part of Schmid tensor given by $0.5(\mathbf{b}^{s(r)} \otimes \mathbf{n}^{s(r)} + \mathbf{n}^{s(r)} \otimes \mathbf{b}^{s(r)})$, where, $\mathbf{b}^{s(r)}$ is the Burgers vector and $\mathbf{n}^{s(r)}$ is the plane normal. The strain rate deviator in grain r is calculated by summing the contributions from all slip systems:

$$\dot{\boldsymbol{\varepsilon}}_{vp}^{(r)} = \sum_s \mathbf{m}^{s(r)} \dot{\gamma}^{s(r)}. \tag{2}$$

Linearization of Eq. (2) gives:

$$\dot{\boldsymbol{\varepsilon}}_{vp}^{(r)} = \mathbf{M}^{(r)} \boldsymbol{\sigma}'^{(r)} + \dot{\boldsymbol{\varepsilon}}^{0(r)}, \tag{3}$$

where $\mathbf{M}^{(r)}$ is local visco-plastic compliance and $\dot{\boldsymbol{\varepsilon}}^{0(r)}$ is the back-extrapolated strain rate in grain r. The linearized moduli, $\mathbf{M}^{(r)}$ and $\dot{\boldsymbol{\varepsilon}}^{0(r)}$, depend on the selected linearization procedure [31]. The n-effective formulation is used in the present work [32]. Each linearized grain is assumed to be a visco-plastic ellipsoidal inhomogeneity within a homogeneous medium that has the homogenized properties of the linearized aggregate [31]. The homogenized effective behavior of the linearized polycrystalline aggregate is:

$$\dot{\boldsymbol{\varepsilon}}_{vp} = \mathbf{M}\boldsymbol{\sigma}' + \dot{\boldsymbol{\varepsilon}}^0, \tag{4}$$

where $\dot{\boldsymbol{\varepsilon}}_{vp}$ and $\boldsymbol{\sigma}'$ are the macroscopic strain rate and stress deviators, $\mathbf{M}$ is the effective visco-plastic compliance, and $\dot{\boldsymbol{\varepsilon}}^0$ is the effective back-extrapolated term. The effective properties are calculated as volume averages of the corresponding local properties weighted by the stress concentration tensors, $\mathbf{B}^{(r)}$ and $\mathbf{b}^{(r)}$:

$$\mathbf{M} = \langle \mathbf{M}^{(r)} \mathbf{B}^{(r)} \rangle, \tag{5}$$

$$\dot{\boldsymbol{\varepsilon}}^0 = \langle \mathbf{M}^{(r)} \mathbf{b}^{(r)} + \dot{\boldsymbol{\varepsilon}}^{0(r)} \rangle, \tag{6}$$

where denotes volume average over the polycrystal. The self-consistent equations Eq. (5)-(6) are solved iteratively using a fixed point method [31].

In the present work, the strain-rate sensitivity of stress is primarily accounted for through the functional dependence of slip resistance on

strain rate, $\tau_c^s(\dot{\varepsilon})$. The strain rate sensitivity of a polycrystalline material is a consequence of two dislocation glide rate effects. First, the slip resistance at a given constant dislocation density (i.e. constant structure) is rate dependent and, second, the evolution of the dislocation density (i.e. evolving structure) is also rate dependent [33]. Since in the present model the functional dependence of slip resistance with strain rate and with rate sensitive dislocation density completely describes the strain rate sensitivity of the material, the contribution to the overall rate sensitivity coming from the power law (Eq. (1)) should be removed or at least minimized. Removal of the power-law rate sensitivity is achieved only for the limit of n approaching infinity ($n \to \infty$). In this case, the strain rate sensitivity of a material response will be solely governed by the slip resistance $\tau_c^s(\dot{\varepsilon})$. The analysis in the previous work [19] showed that a strain-rate sensitivity introduced by n of approximately 400 ($m \approx 0.0025$, $n = 1/m$) is sufficiently low and acceptable for the current application. A further increase of rate exponent results in relatively insignificant improvements.

The VPSC algorithm relies on numerical solution of the constitutive Eq. (2) for grain stress, $\boldsymbol{\sigma}^{(r)}$, in each grain and at every iteration and trial strain increment. This set of equations becomes highly nonlinear and stiff with an increase of rate exponent n beyond 50-100, leading to convergence difficulties in the Newton-Raphson solver. Several alternative non-iterative schemes have been developed to circumvent this issue [24, 34-39]. In addition, in previous work [19, 40] an alternative scheme for reduction of power-law rate sensitivity, referred to as the k-modification (k-mod) method, was proposed and applied within the FE framework. The method is based on modifying the magnitude of the true applied strain-rate, $\dot{\boldsymbol{\varepsilon}}_{vp}^{app}$, before performing the VPSC homogenization. Increase of rate exponent beyond 50 does not appreciably change the slip activity, and thus does not change the direction of strain rate or stress. Therefore, any further increase of rate exponent will mostly affect only the magnitude of the stress. In order to achieve the same effect in terms of stress magnitudes, modification of the applied strain rate is proposed. The modified strain-rate, $\dot{\boldsymbol{\varepsilon}}_{vp}$, is defined as:

$$\dot{\boldsymbol{\varepsilon}}_{vp} = \frac{\dot{\boldsymbol{\varepsilon}}_{vp}^{app}}{|\dot{\boldsymbol{\varepsilon}}_{vp}^{app}/\dot{\varepsilon}_{ref}|} |\dot{\boldsymbol{\varepsilon}}_{vp}^{app}/\dot{\varepsilon}_{ref}|^{\frac{1}{k+1}}, \tag{7}$$

where $\dot{\varepsilon}_{ref} = 1$ /s normalizes the applied strain-rate for consistency of units. The inverse relationship is:

$$\dot{\boldsymbol{\varepsilon}}_{vp}^{app} = \dot{\boldsymbol{\varepsilon}}_{vp} |\dot{\boldsymbol{\varepsilon}}_{vp}/\dot{\varepsilon}_{ref}|^{k}. \tag{8}$$

Eqs. (7) and (8) imply that $|\dot{\boldsymbol{\varepsilon}}_{vp}|$ approaches unity as k increases. In order to understand the effect of the proposed modification, consider the case where the applied strain rate, $\dot{\boldsymbol{\varepsilon}}_{vp}^{app}$, is scaled as $\lambda\dot{\boldsymbol{\varepsilon}}_{vp}^{app}$. From Eq. (7), the strain-rate imposed to the VPSC is $\lambda^{\frac{1}{k+1}}\dot{\boldsymbol{\varepsilon}}_{vp}$. Scaling of macroscopic strain rate results in scaling of grain strain rates $\lambda^{\frac{1}{k+1}}\dot{\boldsymbol{\varepsilon}}_{vp} = \lambda^{\frac{1}{k+1}}\dot{\boldsymbol{\varepsilon}}_{vp}^{(r)}$, where denotes the volume average. Consequently, from Eqs. (1-2) it is clear that the stresses scale as $\lambda^{\frac{1}{(k+1)n}}\boldsymbol{\sigma}' = \lambda^{\frac{1}{(k+1)n}}\boldsymbol{\sigma}'^{(r)}$. Therefore, the proposed modification of the applied strain rate does not affect the directions of the local or macroscopic quantities, which are defined by n. The proposed modification only affects the magnitudes of the quantities, causing a decrease in rate sensitivity, m, with increase of k, which is now defined as combination of both n and k: $m = 1/((k+1)n)$.The k-mod method does not influence the computational time of the VPSC solution procedure, which is only influenced by the power-law exponent n. Moreover, k does not influence the relative activity of deformation systems. Based on previous work [19], for the simulations in the present work we adopt $k = 7$ and $n = 50$, resulting in rate sensitivity of $m = 1/(n(k+1)) = 1/400$.

After VPSC has converged, the shearing rates $\dot{\gamma}^{s(r)}$ have to be re-scaled for $|\dot{\boldsymbol{\varepsilon}}_{vp}/\dot{\varepsilon}_{ref}|^k$, so that the total shear corresponds to the true, applied strain rate. Next, shear rates are used for calculation of the crystal lattice rotation rates, $\mathbf{W}^{*(r)}$, in each grain, r:

$$\mathbf{W}^{*(r)} = \mathbf{W} + \boldsymbol{\Pi}^{(r)} - \mathbf{W}^{p(r)}, \tag{9}$$

where $\mathbf{W}$ is an applied spin tensor, $\boldsymbol{\Pi}^{(r)}$ is an inclusion spin [31], and $\mathbf{W}^{p(r)}$ is the plastic spin tensor given by:

$$\mathbf{W}^{p(r)} = 0.5 \sum_s \dot{\gamma}^{s(r)}(\mathbf{b}^{s(r)} \otimes \mathbf{n}^{s(r)} - \mathbf{n}^{s(r)} \otimes \mathbf{b}^{s(r)}). \tag{10}$$

Standalone VPSC is used to simulate relatively simple, usually monotonic, deformation processes such as simple tension, compression, and shear. Since heterogeneous mechanical fields develop in more complicated mechanical tests (e.g. beam bending or impact tests) and during metal forming process [41-47], it is necessary to couple VPSC with a FEM framework. The constitutive response at every material/integration point is obtained through VPSC homogenization of a polycrystalline aggregate. The FE-VPSC coupling strategy used in this work was first described in [48] and then advanced in terms of numerical methods and efficiency in [18, 23]. The coupled model has been successful in simulating bimetallic tube extrusion [26], bending [49], rolling [21, 50], impact [18] and behavior of certain structural components [51].

The FE-VPSC model utilizes the following rate constitutive equation for total stress rate in the global frame [30, 52-56]:

$$\dot{\boldsymbol{\sigma}} = \langle \hat{\dot{\boldsymbol{\sigma}}}^{(r)} \rangle + \langle \mathbf{W}^{*(r)}\boldsymbol{\sigma}^{(r)} - \boldsymbol{\sigma}^{(r)}\mathbf{W}^{*(r)} \rangle = \langle \mathbf{C}^{(r)}(\dot{\boldsymbol{\varepsilon}} - |\dot{\boldsymbol{\varepsilon}}_{vp}/\dot{\varepsilon}_{ref}|^k \dot{\boldsymbol{\varepsilon}}_{vp}) \rangle + \langle \mathbf{W}^{*(r)}\boldsymbol{\sigma}^{(r)} - \boldsymbol{\sigma}^{(r)}\mathbf{W}^{*(r)} \rangle, \tag{11}$$

where $\hat{\dot{\boldsymbol{\sigma}}}^{(r)}$ is the Jaumann stress rate and $\mathbf{C}^{(r)}$ is the elastic stiffness of grain r. In Eq. (11), the Cauchy stress rate, $\dot{\boldsymbol{\sigma}}$, is defined at every FEM integration point as the volume average over all grains. In addition, Eq. (7) has been substituted for the applied viscoplastic strain rate. Integration of equation Eq. (11) using the Euler backward method leads to the following expression for stress at the end of a time increment [19, 57]:

$$\boldsymbol{\sigma}^{t+\Delta t} = \mathbf{C}\left(\Delta\boldsymbol{\varepsilon} - \left|\frac{\dot{\boldsymbol{\varepsilon}}_{vp}}{\dot{\varepsilon}_{ref}}\right|^k \dot{\boldsymbol{\varepsilon}}_{vp}\Delta t\right) + \langle \Delta\mathbf{R}^{*(r)}\boldsymbol{\sigma}^{(r),t}\Delta\mathbf{R}^{*(r)T} \rangle, \tag{12}$$

where $\mathbf{C}$ is the elastic self-consistent stiffness, $\Delta\boldsymbol{\varepsilon}$ and Δt are strain and time increments, and $\Delta\mathbf{R}^{*(r)}$ is the increment in rotation calculated from $\mathbf{W}^{*(r)}$. Eq. (12) is solved for $\dot{\boldsymbol{\varepsilon}}_{vp}$ using Newton's method [19]. In addition to stress, the global FEM solver requires the Jacobian matrix at each integration point [58]. For the above constitutive equation, the details on the solution procedure and the semi-analytical Jacobian can be found in [19].

The coupled model relies on a hardening law for the evolution of slip resistances, τ_c^s, with plastic slip (γ^s), temperature (T) and strain-rate ($\dot{\varepsilon}$). A thermally-activated dislocation density-based hardening law is used in the present work [59]. The resistances to twinning modes are not functions of strain-rate and temperature directly but indirectly based on slip-twin interactions. Grain re-orientation due to twinning is modeled using the simplified composite grain (CG) model where twins are treated as separate grains and not as part of the grain parent composite [60]. A summary of the equation pertaining to the evolution of slip and twin resistances is given in appendix A. The specific version of the hardening law for Zr has been calibrated and validated in earlier works [19, 61].

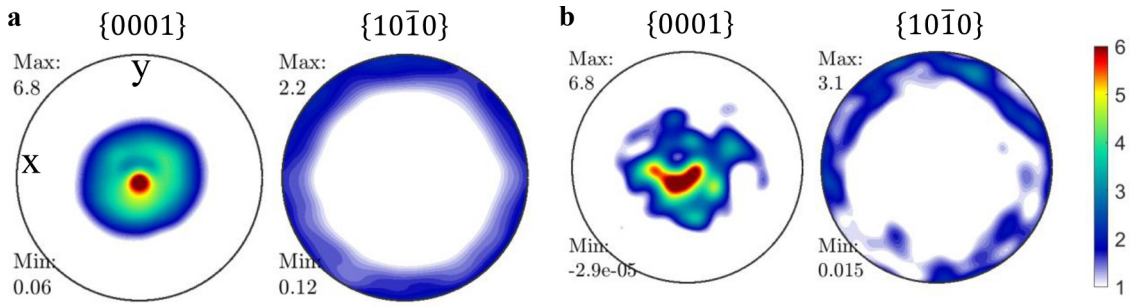

Fig. 1. Pole figures representing the initial texture of the Zr plate after clock-rolling and annealing: (a) obtained experimentally by diffraction and (b) approximated with 150 weighted crystal orientations for use in simulations.

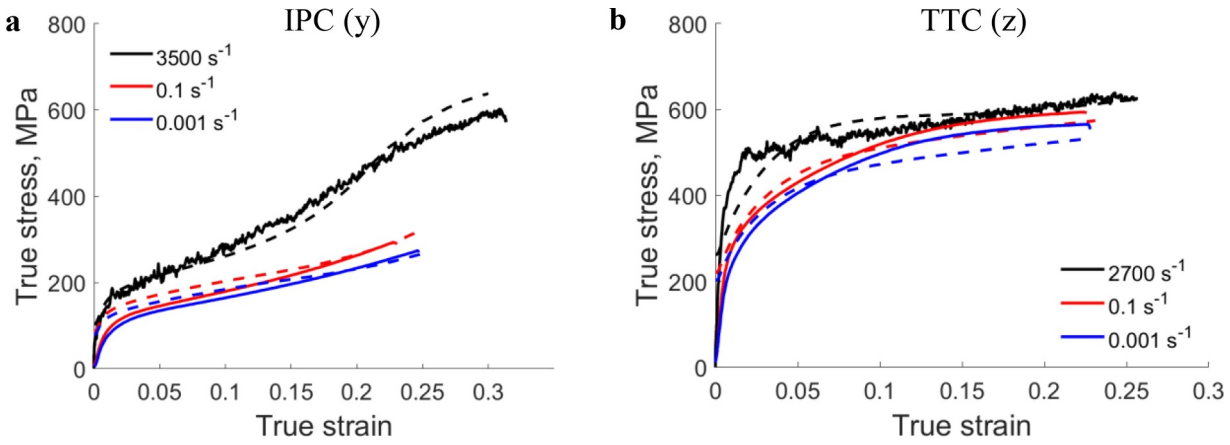

Fig. 2. Comparison of measured (solid lines) and VPSC simulated (dashed lines) true stress-true strain curves for Zr in compression at room temperature as a function of strain rate along: (a) in-plane direction (IPC or y) and (b) through-thickness direction (TTC or z). The simulated results based on the measured texture with a full set of crystal orientations and the corresponding texture represented with 150 weighted crystal orientations are nearly identical.

3. Results and discussion

3.1. Model calibration

The modeling framework is evaluated in the present work on a comprehensive data set in terms of capturing geometrical changes and microstructural evolution across strain rates and temperatures. The texture of the high-purity, clock rolled and annealed Zr plate is shown in Fig. 1. The in-plane 1 (IP1 = x) direction was the final rolling direction for the plate, while the in-plane 2 (IP2 = y) is the direction perpendicular to IP1 within the plane of the plate. The remaining plate direction is the through-thickness (TT = z) direction. As can be seen, the Zr plate has a strong basal texture. We approximate the measured orientation distribution function (ODF), defined by 1944 weighted crystal orientations, with 150 weighted orientations.

The plasticity of Zr is carried out using the following slip modes: prismatic {$\bar{1}$100} < $\bar{1}\bar{1}$20>, pyramidal type I {10$\bar{1}$1} < $\bar{1}\bar{1}$23>, and basal {0001} < $\bar{1}\bar{1}$20> [62-64]; and twinning modes: extension {10$\bar{1}$2} < 10$\bar{1}\bar{1}$> and {11$\bar{2}$1} < 10$\bar{2}$6> and contraction {11$\bar{2}$2} < 11$\bar{2}\bar{3}$> and {10$\bar{1}$1} < 10$\bar{1}\bar{2}$> [65-67]. While the first extension and contraction twins activate in large fractions, minor contents of the second extension and the second contraction twins are also observed and thus are considered in the simulations. These have been made available in the model for completeness. The consideration of {11$\bar{2}$1} < 10$\bar{2}$6> twin results in a minor difference between the present model and the one used in earlier works [19, 61].

The variety of tests performed for Zr facilitate detailed characterization of model parameters and testing of the model performances. Simple compression and tension tests are used to calibrate and validate the model parameters under simple boundary conditions but for different strain rates and temperatures. This was done in our earlier works [19, 61]. However, given the further optimization of material parameters performed in this work, the simulations are rerun for verification. Given the starting texture, the in-plane and through thickness compression tests are simulated at room temperature for strain rates ranging from 0.001 /s to 3500 /s. The comparison with measurements is shown on Fig. 2. Simple compression VPSC simulations were run using both the full texture and the approximated texture to quantify the difference in simulation results. The difference was approximately 3%. In terms of additional validation of model parameters under simple compression, Fig. 3 shows a comparison of calculated and measured [68] local twin fractions for the central sample surface after simple compression at liquid nitrogen temperature (i.e. 77 K) to a strain of 8.9 % under a strain rate of 10^{-3} s^{-1}. For further validation in terms of capturing geometrical changes and microstructural evolution, the quasi-static beam bending tests are used. Here, more complex

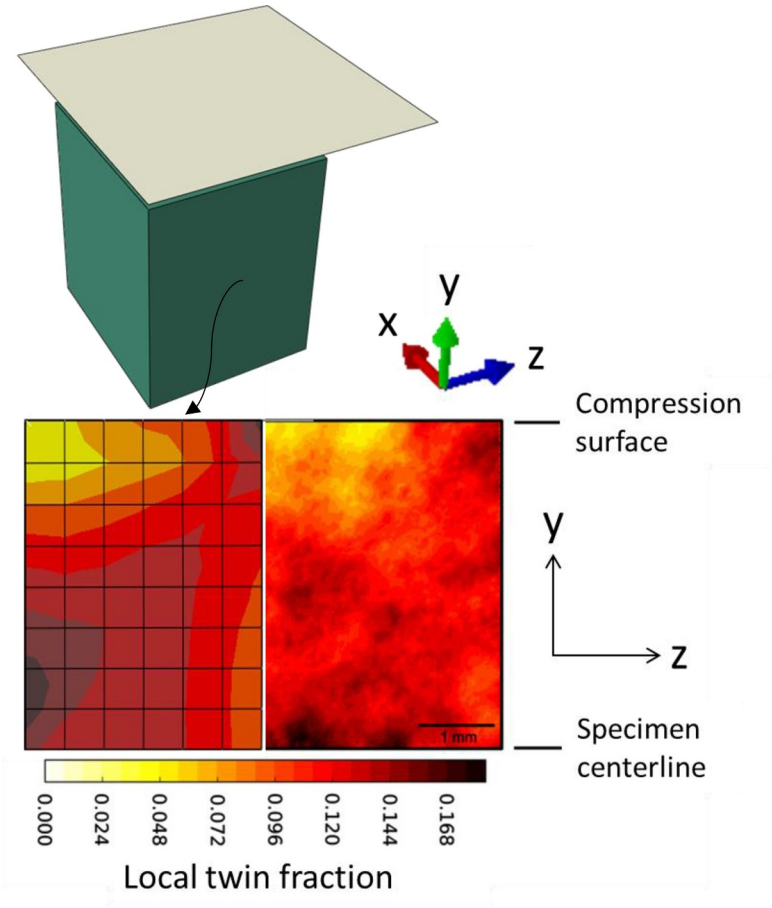

Fig. 3. Comparison of calculated and EBSD measured [68] local twin fractions for the ½ in y and ½ in z area, which is the central sample surface (i.e. ½ in x) after simple compression to a strain of 8.9 % at 77 K and a strain rate of $10^{-3}\,s^{-1}$. The initial sample was a cube with the following dimensions: 7.8 mm along x (IP1), 8.8 mm along y (IP2), and 6.8 mm along z (TT). 1/8 (i.e. ½ in x, ½ in y, and ½ in z) FE model is also shown. The compression simulation was performed with a friction coefficient of $\mu = 0.1$.

Table. 1
Slip system hardening law parameters for Zr.

Parameter	Slip mode, α		
	$\{\bar{1}100\} < \bar{1}\bar{1}20>$	$\{10\bar{1}1\} < \bar{1}\bar{1}23>$	$\{0001\} < \bar{1}\bar{1}20>$
b^{α}, m	3.231×10^{-10}	6.0771×10^{-10}	3.231×10^{-10}
τ_0^{α}, MPa	$\tau_0^{\alpha} = A(1 + B\log(\frac{\dot{\varepsilon}}{\dot{\varepsilon}_{ref}}))\exp(-\frac{T}{C})(1 + E\ lognormal(\sigma, \nu))$		
HP^{α}	0.1	0.17	0.1
k_1^{α}, m^{-1}	5.3×10^{8}	2.0×10^{9}	9.7×10^{8}
g^{α}	0.002	0.005	0.002
D^{α}, MPa	700	1400	1400
q^{α}	$12\log(1 + T/30)$	0.1	$12\log(1 + T/30)$
A^{α}, MPa	23.5	350	2500
B^{α}	0.04	0.02	N/A
C^{α}, K	235	190	150
E^{α}	6900	36000	N/A
ν^{α}	7.2	7.45	N/A
σ^{α}	0.5	0.5	N/A

deformation develops ranging from compression to tension across the beam thickness. The Taylor impact tests are used to optimize and verify the model parameters in the high strain rate regimes. The strain-rate fields for the Taylor impact test can be orders of magnitude greater than the strain-rates achieved during the split Hopkinson pressure bar testing. Therefore, the standalone VPSC model validation from the split Hopkinson pressure bar tests shown on Fig. 2 and underlying micro-structural evolution can be regarded only as a first-level validation. Nevertheless, model validation using split Hopkinson pressure bar testing data is commonly performed before simulating full-scale Taylor impact tests. In particular, the earlier established parameters for twinning are further optimized to extrapolate the predictive behavior of the model to higher strain-rates, as will be described shortly. Tables 1 and 2 present the complete list of hardening parameters for Zr. Additionally, the elastic constants used in calculating the elastic stiffness tensor are: $C_{11} = 143,500$ MPa, $C_{33} = 164,900$ MPa, $C_{12} = 72,500$ MPa, and $C_{13} = 65,400$ MPa, $C_{44} = 32,100$ MPa

Table. 2
Twin system hardening law parameters for Zr.

Parameter	Twinning mode, β			
	$\{10\bar{1}2\} < 10\bar{1}\bar{1}>$	$\{11\bar{2}1\} < 10\bar{2}6>$	$\{11\bar{2}2\} < 11\bar{2}\bar{3}>$	$\{10\bar{1}1\} < 10\bar{1}\bar{2}>$
b^{β}, m	6.33×10^{-11}	9.68×10^{-11}	9.24×10^{-11}	3.0796×10^{-11}
S	0.167	0.6277	0.225	0.104
τ_{crit}^{β}, MPa	100	300	230	350
τ_{prop}^{β}, MPa	5	300	230	50
HP^{β}, MPa/$\sqrt{m}$	0.135	0.1	0.1	0.1
$C^{1\beta}$	N/A	N/A	$1300 - 100\log(\frac{\dot{\varepsilon}}{\dot{\varepsilon}_{ref}})$	N/A
$C^{2\beta}$	100	N/A		N/A
$C^{3\beta}$	N/A	N/A	$1300 - 100\log(\frac{\dot{\varepsilon}}{\dot{\varepsilon}_{ref}})$	N/A

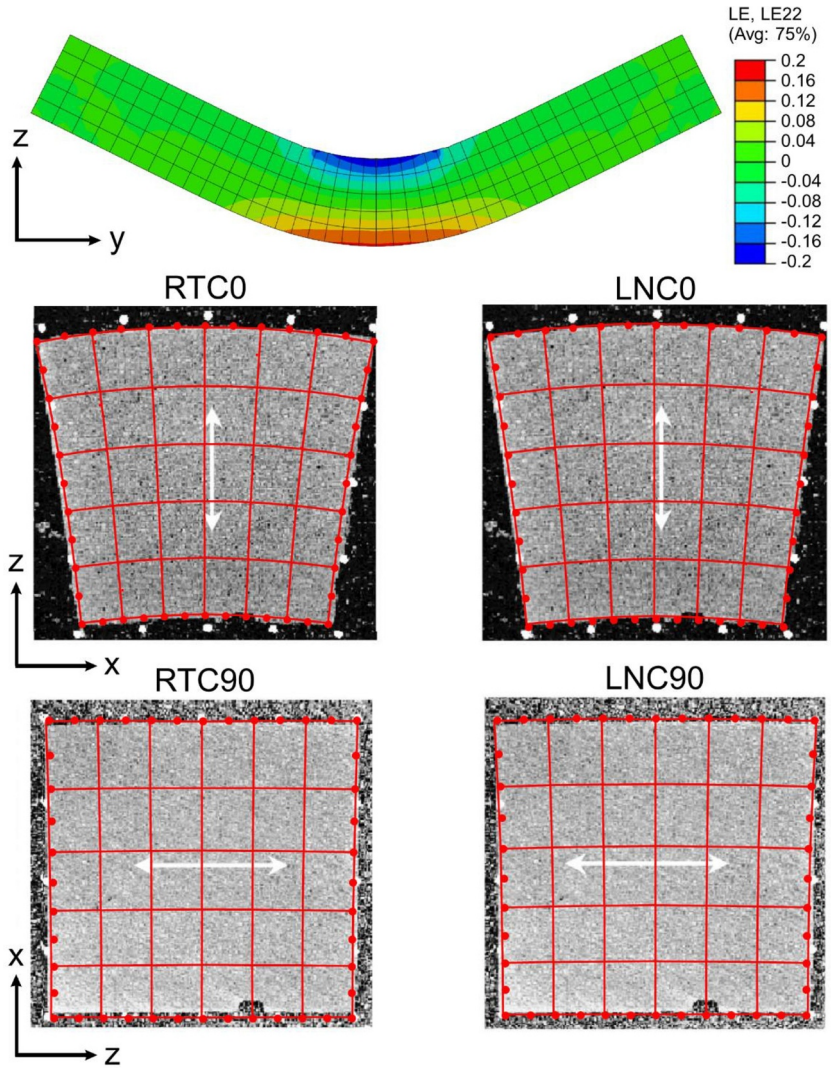

Fig. 4. Comparison of the measured (photographs) [28] and predicted (mesh consisting of the quadratic elements with reduced integration (C3D20R) along with the external nodal coordinates) mid-cross-sectional geometries of the Zr beams deformed under quasi-static deformation conditions. The FE model on top shows axial strain contours. The adopted frame is defined relative to the Zr plate as follows: x = IP1, y = IP2 and z = TT.

C_{66} = 35, 500 MPa [69].

3.2. Bending tests of Zr

Four-point beam bending tests were carried out on a setup/fixture consisting of a pair of internal pins (center-to-center distances, y = ± 6.35 mm) displaced downwards from the top and a pair of external pins (center-to-center distances, y = ± 12.7 mm) fixed at the bottom of the beam [28]. To facilitate bending, the upper pins moved 6 mm downward. The beams of Zr for the bending tests had an initial square cross-section of 6.35 mm edge length and were 50.8 mm in length along the plate in-plane 2 (IP2 = y) direction. Two beams were bent along TT = z and two along IP1 = x; one beam per category was bent at room temperature (RT) and another at liquid nitrogen (LN) temperature. The two test configurations (designated as 0 and 90, respectively) at two temperatures (RT and LN) facilitate evaluating the model's capability to capture the effects of texture and temperature on anisotropic material flow. After bending, the textures of the beams were measured and the shapes of the beams were photographed. The bent specimens were cut axially in the middle in order to photograph the cross-sections. These photographs are used here to evaluate the accuracy of the FE-VPSC model for Zr. The data pertaining to the beams with more details was presented in [28]. To simulate the bending conditions, a 3D model was created in the Abaqus FEM software package. A quarter model of the beam was meshed with C3D20R structural elements with 20 × 5 × 3 discretization along length, thickness, and half-width, respectively. Because of the orthotropic symmetry of the Zr plate, symmetry boundary conditions were imposed. Consistent with experiments, the displacement was - 6 mm. The Abaqus standard implicit FEM solver along with the FE-VPSC User MATerial (UMAT) subroutine was utilized for the simulations. Every integration point of the FEM model was a VPSC polycrystalline

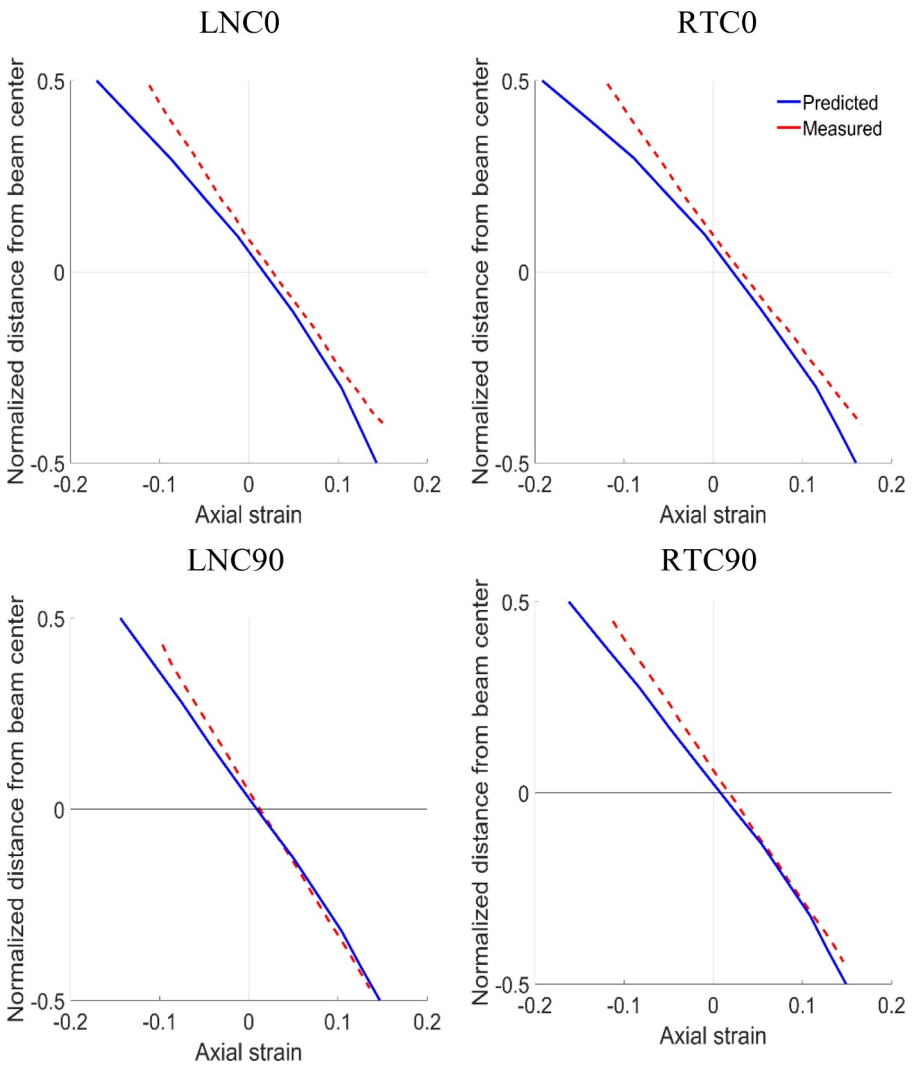

Fig. 5. Measured [28] versus predicted axial strain along the height of the beams. Shift of the neutral axis varies due to the anisotropic material flow amongst the beams.

aggregate of 150 weighted orientations approximating the texture of the Zr plate.

Fig. 4 shows the comparison between measured and predicted cross sections after bending. The figure on top shows the example of the axial strain distribution for the LNC0 case, and all of the other configurations look similar. In the cross-section images, external nodes are overlaid on the photographs. As is evident, the FE-VPSC model captures the dimensional changes with great accuracy. The shape changes are primarily a consequence of the anisotropy of the Zr plate due to texture. When the TT (z) is along the loading direction, the deformed beams develop typical wedge-shape cross sections. However, when the TT (z) is perpendicular to the loading direction, the cross-sections of the beams remain almost square. The latter is associated with the relative difficulty to deform grains along the **c**-axis. Looking at Fig. 2, simple compression tests show that the TT direction is stronger than the IP directions for the Zr plate. Fig. 5 shows a comparison between measured and predicted shifts in the neutral axis of the beams. The shifts are a consequence of the anisotropic material flow. Finally, Fig. 6 shows predicted texture evolution after the bending. Comparison with experimental textures from [28] reveals good agreement. When the beam is in compression axially in y, there are peaks in the pole figures due to extension twinning. In particular, the twinning signatures in LNC0 and LNC90 are in the regions where many grains are in compression perpendicular to their **c**-axis flipping grain's **c**-axes from z towards the compression direction, which is y.

3.3. Taylor impact cylinder tests of Zr

Due to large gradients in deformation conditions, the Taylor impact cylinder test provides a wealth of spatially varying microstructural data, along with the evolution of sample geometry, and is thus suitable for evaluating material models. The post-deformation microstructural changes in terms of texture and development of deformation twins can be measured. The Zr cylinders for the impact tests in the present work have diameters of 7.62 mm and lengths of 50.8 mm with the axis along the plate in-plane 2 (IP2 = y) direction. During the impact tests,

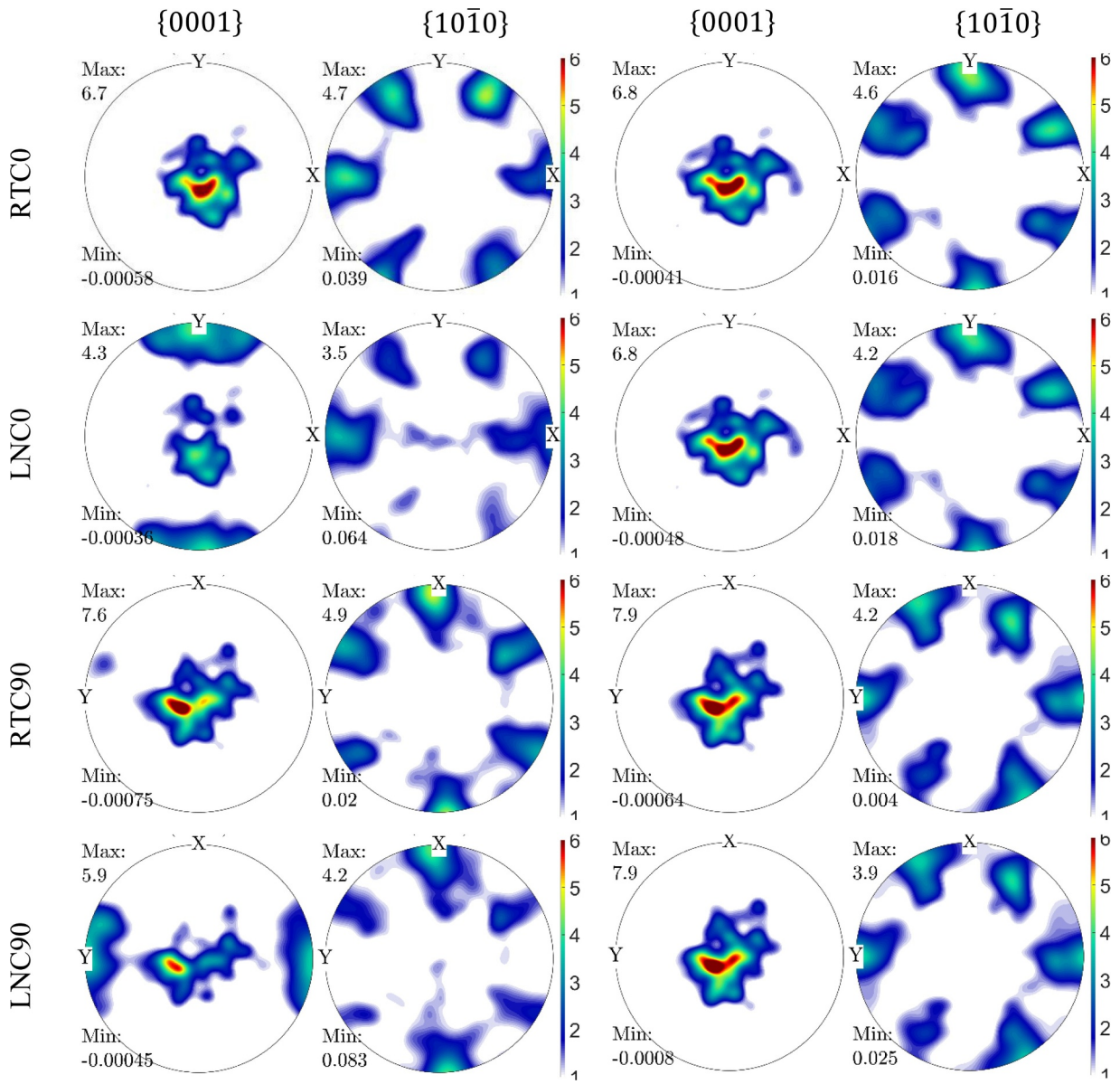

Fig. 6. Pole figures predicted by FE-VPSC visualizing texture evolution after bending at the top (left column) and the bottom (right column) of the beams at their axial mid locations. The adopted frame is defined relative to the Zr plate as follows: x = IP1, y = IP2 and z = TT.

cylinders were shot at a rigid steel wall. After the impact, shapes of the cylinders were measured and microstructures were characterized by EBSD at different locations along the axial direction of the mid plane. To simulate the impact test, a 3D model was created in the Abaqus FEM software package as depicted in Fig. 7. Due to symmetry of the geometry and initial microstructure, a quarter of the cylinder was simulated and discretized into 405 C3D8 elements. A coarser mesh was used close to the tail of the cylinder due to the small amount of deformation in this region. The wall was simulated as a fixed rigid plane. Consistent with experiments, 100 m/s, 170 m/s, and 243 m/s initial velocities were applied to the cylinders. The Abaqus dynamic implicit FEM solver along with the FE-VPSC User MATerial (UMAT) subroutine was utilized for the simulations. Density of $\rho = 6520$ kg/m^3 for Zr was used to model the inertia effects. Every integration point of the FEM model was a VPSC polycrystalline aggregate of 150 weighted orientations approximating the texture of the Zr plate. FE-VPSC predictions of post-impact geometry, texture, and twin volume fraction are compared with the experimental measurements.

Fig. 8 shows the evolution of equivalent plastic strain rate fields during impact for each cylinder. The selected states of the cylinders are presented at identical times, except the last state, which is the simulation time at the end of deformation. After this end of deformation

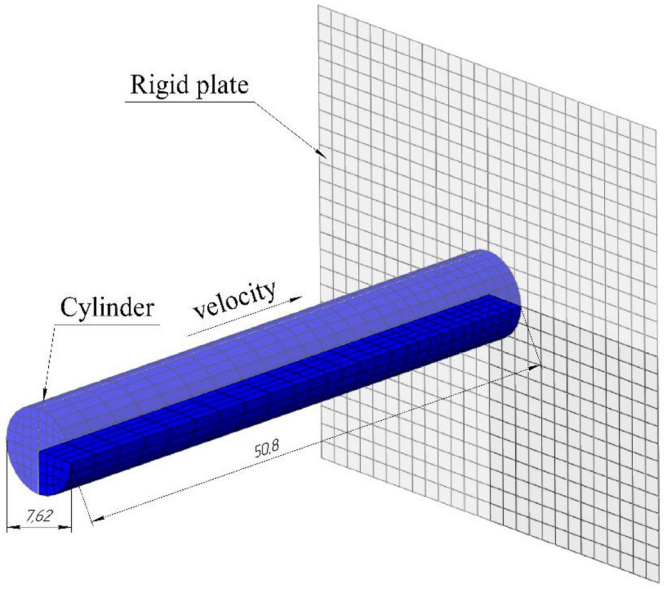

Fig. 7. ¼ FEM model consisting of 405 continuum 3D eight-nodal (C3D8) elements for simulating the Taylor cylinder impact tests. Translucent color represents the original shape of the cylinder, while the opaque color is the quarter model used for the simulations.

time, the cylinder starts bouncing back. It is seen that strain-rate and deformation increase with increasing impact velocity with the former reaching values of up to 160,000 s^{-1}. The deformation is highly heterogeneous and the highest strain occurs at the foot region of the cylinders. At the impact velocities of 170 and 243 m/s, there is necking in the area close to foot, which was also observed in earlier works [27]. The neck is caused by localized tensile loading which is due to the interaction of propagating forward and reflected elastic waves. Additionally, the figure shows equivalent plastic strain (PEEQ) contours after the impact revealing the strain levels in the three cylinders.

The deformed shape and microstructure were measured for the tested cylinders. The post-impact shapes were digitized using the procedure from [11], and are compared with the FE-VPSC predictions in Figs. 9 and 10. As expected, the deformed shapes and extent of plasticity vary among the three tests due to the variation of imposed velocities, with plastic distortions increasing with the impact velocity. The texture and twinning cause the anisotropy of plastic flow. Consequently, initially circular cross-section constant along the cylinder axis becomes elliptical with varying semi-axes along the cylinder axis after the impact (Figs. 9 and 10). The plastic distortions can be further quantified as the ratio between radial strains in the minor and major axes directions (R-value). The R-value slightly decreases with the impact velocity. The deformed regions at lower strain levels display higher R-values (e.g. tail of the 100 m/s cylinder). Generally, the simulated cylinder shapes achieve reasonably good agreement with the

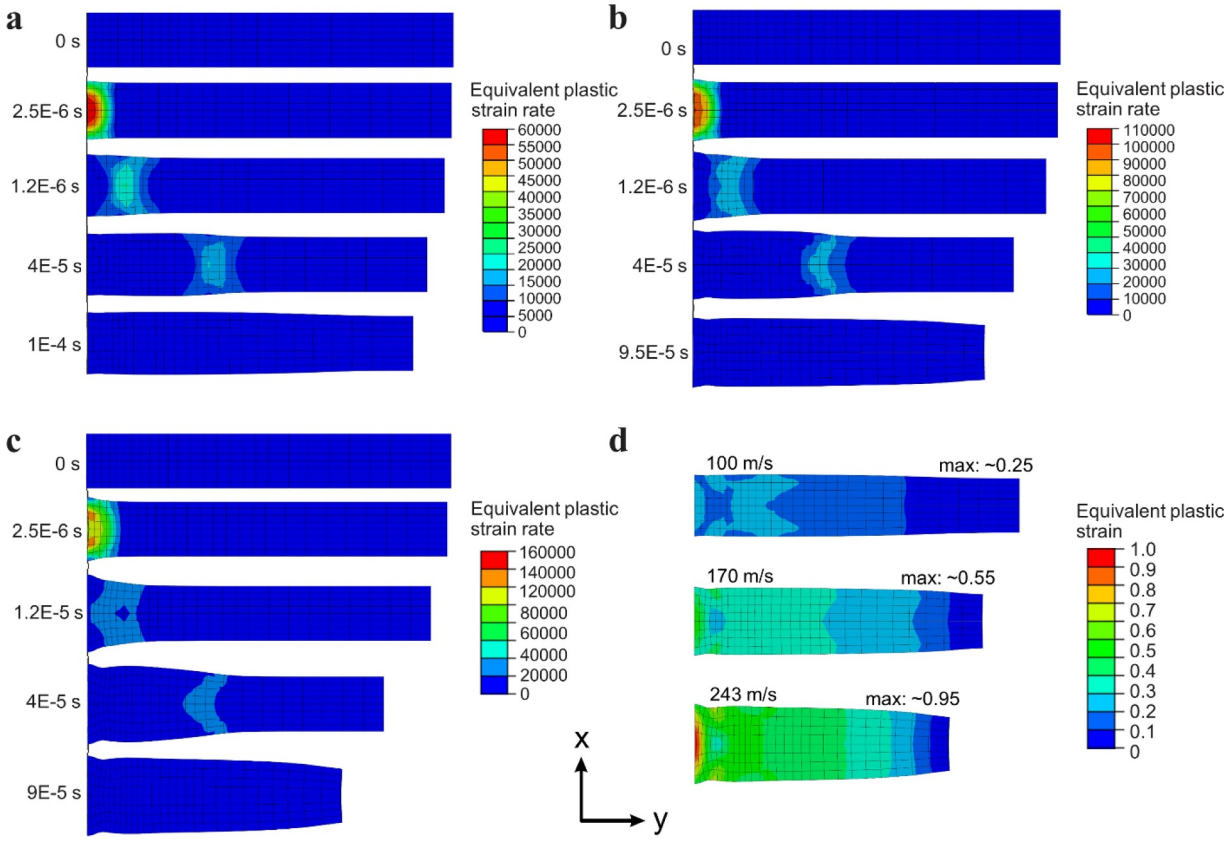

Fig. 8. Equivalent plastic strain-rate fields over the cylinders during their impacts at times indicated in the figure: (a) 100 m/s, (b) 170 m/s, and (c) 243 m/s. (d) Equivalent plastic strain fields after the impact with the largest values indicated per cylinder. Note that the equivalent plastic strain rate scales for the three cylinders are different and divided so the number are round.

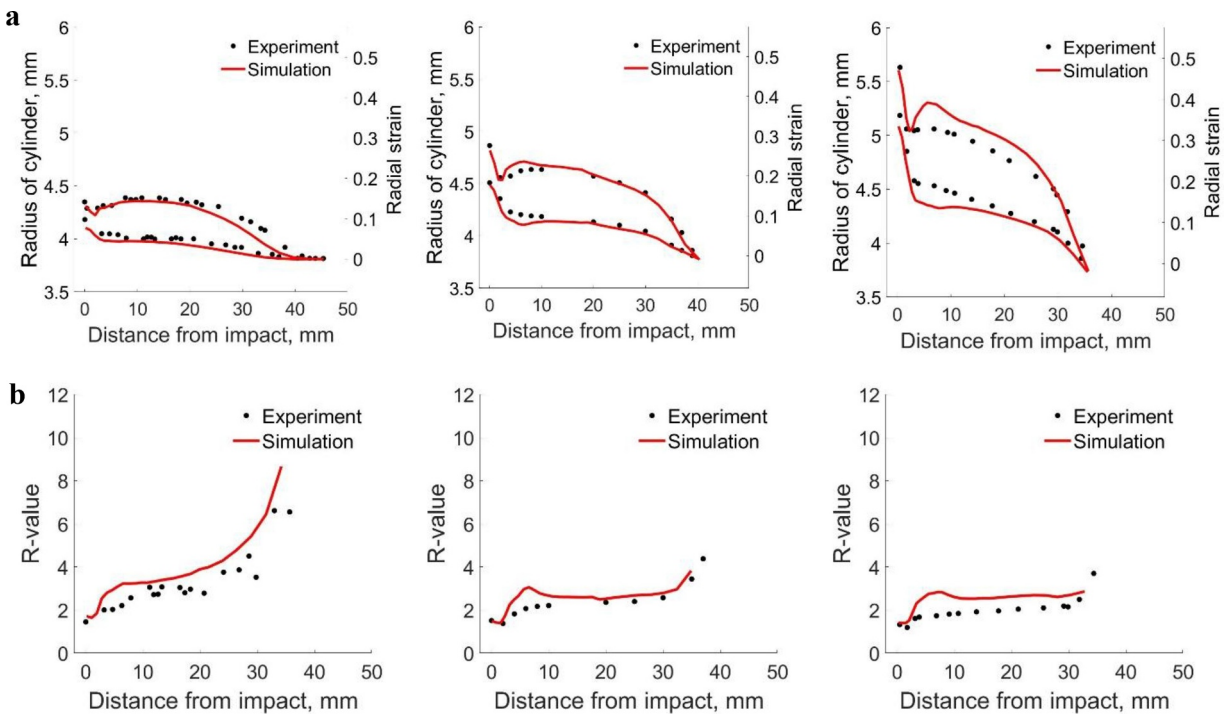

Fig. 9. Plots comparing measured and predicted geometrical changes in terms of (a) radius (major in x and minor in z) along with the major and minor radial strain and (b) R-ratio, which is the ratio between the major and minor radial strains. The plots are after the impacts at 100 m/s (on the left), 170 m/s (middle) and 243 m/s (on the right).

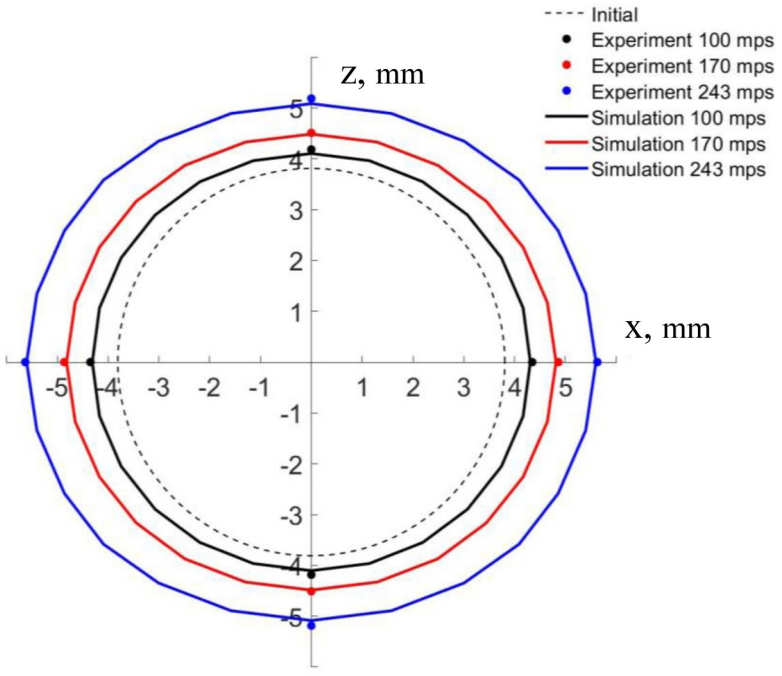

Fig. 10. Comparison of measured and predicted cross-section at the foot region after the impacts at 100 m/s, 170 m/s, and 243 m/s. The initial cross-section is also shown to illustrate the level of deformation from the tail to the foot.

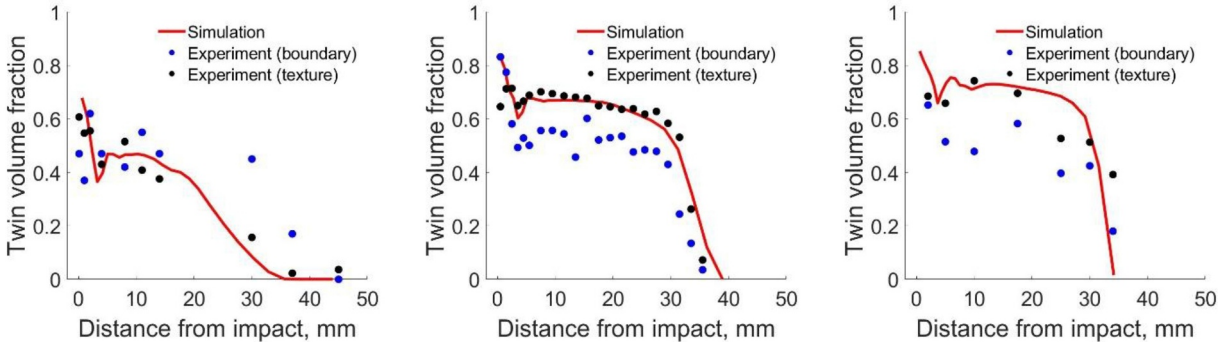

Fig. 11. Plots comparing estimates in measured and predicted evolution of twin volume fraction after the impacts at 100 (on the left), 170 m/s (middle) and 243 m/s (on the right).

measurements. For the 243 m/s cylinder, the distortion in the simulated geometry is slightly over predicted relative to the experimental measurements. This is associated with slightly over predicting twinning as seen in Fig. 11.

We now turn our attention to microstructural evolution under the impact. To this end, appendix B shows a number of inverse pole figure (IPF) maps measured by EBSD at different locations along the axis of the post-impact specimens used for calculation of the twin volume fractions. Due to high deformation in the foot region, quantitative analysis of measured microstructure is challenging. The foot region appears profusely twinned with abundance of primary tensile $\{10\bar{1}2\} < 10\bar{1}\bar{1}>$ twins, presence of secondary compression $\{11\bar{2}2\} < 11\bar{2}\bar{3}>$ twin, and even traces of tertiary twins. Away from the foot, most of the twins are $\{10\bar{1}2\} < 10\bar{1}\bar{1}>$ tensile twins. While deformation twinning was characterized by EBSD using small higher resolution scans, texture evolution was characterized using larger EBSD scans. Twin volume fractions were determined in the EBSD analysis software using the boundary length fraction method and the twinned material area fraction method. Since grains in the foot region appear to be nearly fully consumed by deformation twins, the method based on boundary length fractions in the microstructure is not accurate. Alternatively, the volume fraction of twinned material can be approximated as the volume fraction of material with **c**-axis close to the compression direction. Thus, the twin fractions were also estimated assuming that twins reorient texture toward the loading direction using the texture data from the large scans [70, 71]. A misorientation cutoff of 40-45° between the loading direction and c-axis was used to identify the volume fraction twins. However, both methods are regarded as lower bounds as it is also necessary to account for secondary twins, since the primary twins may also twin. Neither of the twin volume fraction calculation methods predicts that the foot regions for 170 /s and 243 /s cylinders are 100% twinned, as the maps suggest. Consequently, the estimated twin volume fractions at and near the foot region are crude approximations. On the other hand, the estimated twin volume fractions away from the foot are much more reliable. Full twinning would accommodate approximately 10% of the plastic strain in Zr.

Fig. 11 compares measured and predicted twin volume fractions. The accumulated twin volume fraction is the highest at the foot region with a dip slightly away from the foot. The drop arises due to localized tensile deformation conditions caused by the interaction between forward and reflected elastic waves. In dynamic loading, forward and reflected elastic waves encounter each other and cause tensile deformation after they pass by one another. Only the 243 m/s cylinder is plastically deformed along the entire length with some twins even in the tail region. The twin volume fractions along the axis of the cylinders after the impact are predicted with good accuracy. These predictions are based the optimized model parameters. Some optimization was necessary because peaks associated with secondary twinning appeared too pronounced in the texture simulations under high strain-rates of over 100,000 /s. While secondary twinning is experimentally observed, the simulations were over predicting the volume fractions. In order to improve these simulations, secondary twinning needed to be suppressed. To this end, the maximum allowed secondary twin volume fraction was set to 0.1.

Figs. 12-14 show pole figures at different locations along the axial direction of the cylinder after impact for 100 m/s, 170 m/s, and 243 m/s velocities. Higher impact velocity causes larger deformation due to larger inertial forces which can be seen from the evolution of texture and microstructure. As is evident, texture at the foot is sharp and almost completely reoriented primarily by $\{10\bar{1}2\} < 10\bar{1}\bar{1}>$ extension twinning. The texture plots suggest that the 170 m/s and 243 m/s cylinders are nearly 100% twinned at the foot. The basal planes reorient such that the crystallographic **c**-axes aligns with the impact direction, while the prismatic planes form some radial spread. Away from the foot, texture evolution is less dramatic and driven by a combination of slip and twinning. Overall, the model achieves good agreement.

4. Summary and conclusions

Simulations of microstructure and geometry for anisotropic metals with an HCP lattice are challenging, especially under high strain-rate loading conditions. This work utilized a multi-scale model linking crystallography of thermally activated dislocation glide and twinning (~nm), the grain-level plasticity (μm), the VPSC polycrystalline homogenization (mm), and the macro-level plasticity in the FEM (m) to study the mechanical behavior and microstructural evolution of Zr as a function of strain rate. The model treats the strain-rate sensitivity of a material as a consequence of dislocation glide i.e. the evolution of the slip resistance due to microstructural evolution with a realistic value of the visco-plastic power-law exponent governing the constant structure

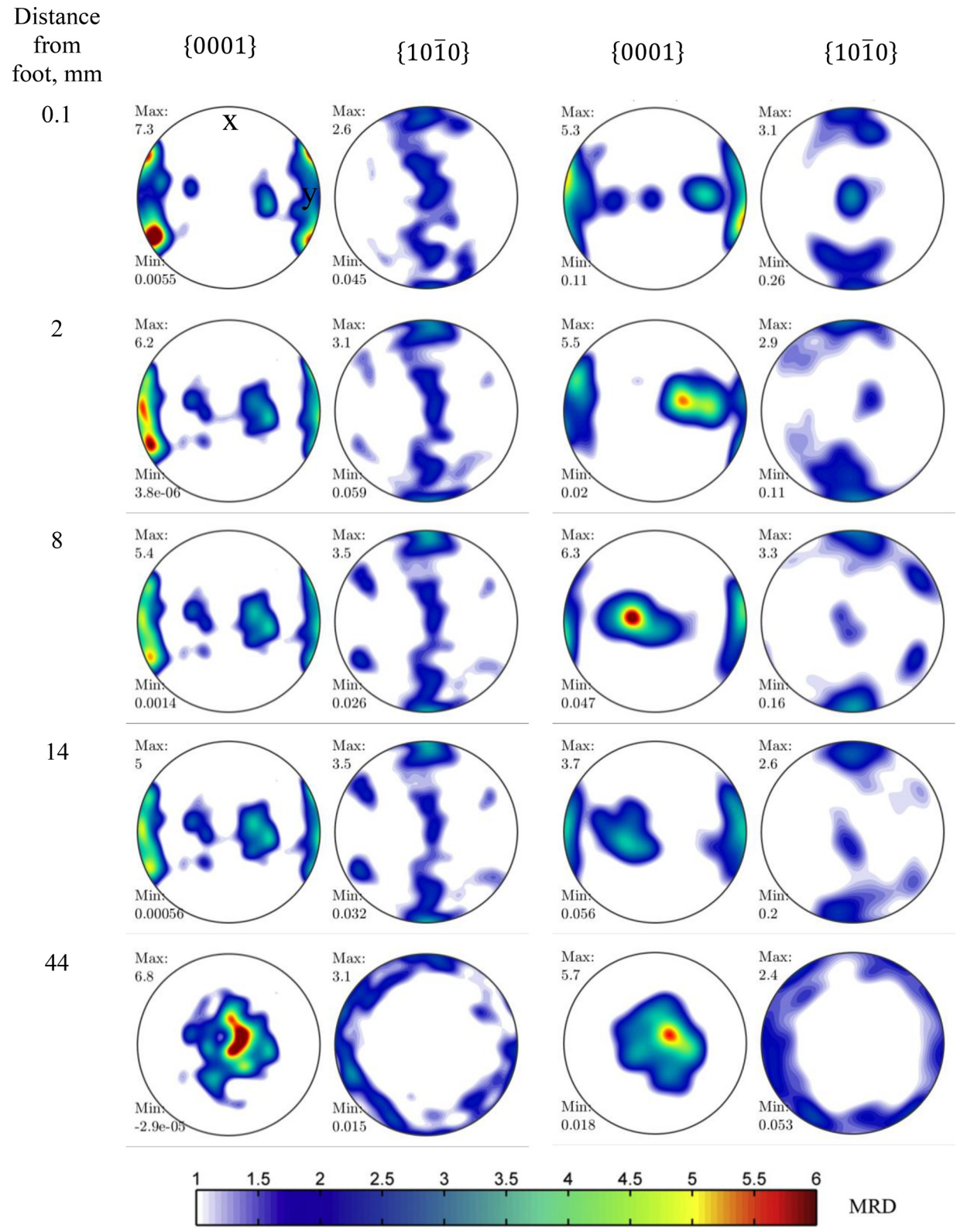

Fig. 12. Pole figures showing the comparison between measure (by EBSD) and predicted texture evolution after the 100 m/s impact as a function of the distance from the foot. The intensity bar is in the multiples of random distribution (MRD).

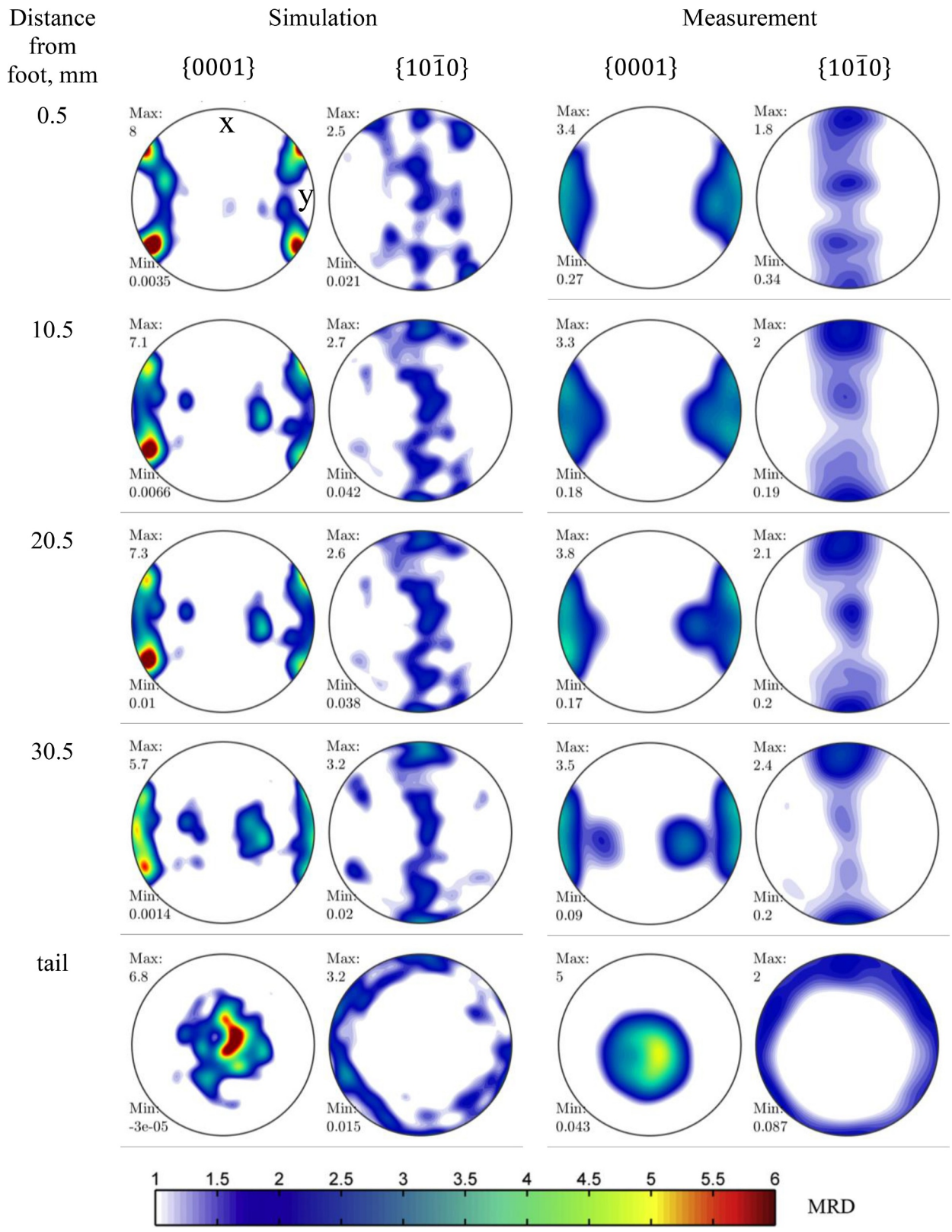

Fig. 13. Pole figures showing the comparison between measure (by EBSD) and predicted texture evolution after the 170 m/s impact as a function of the distance from the foot.

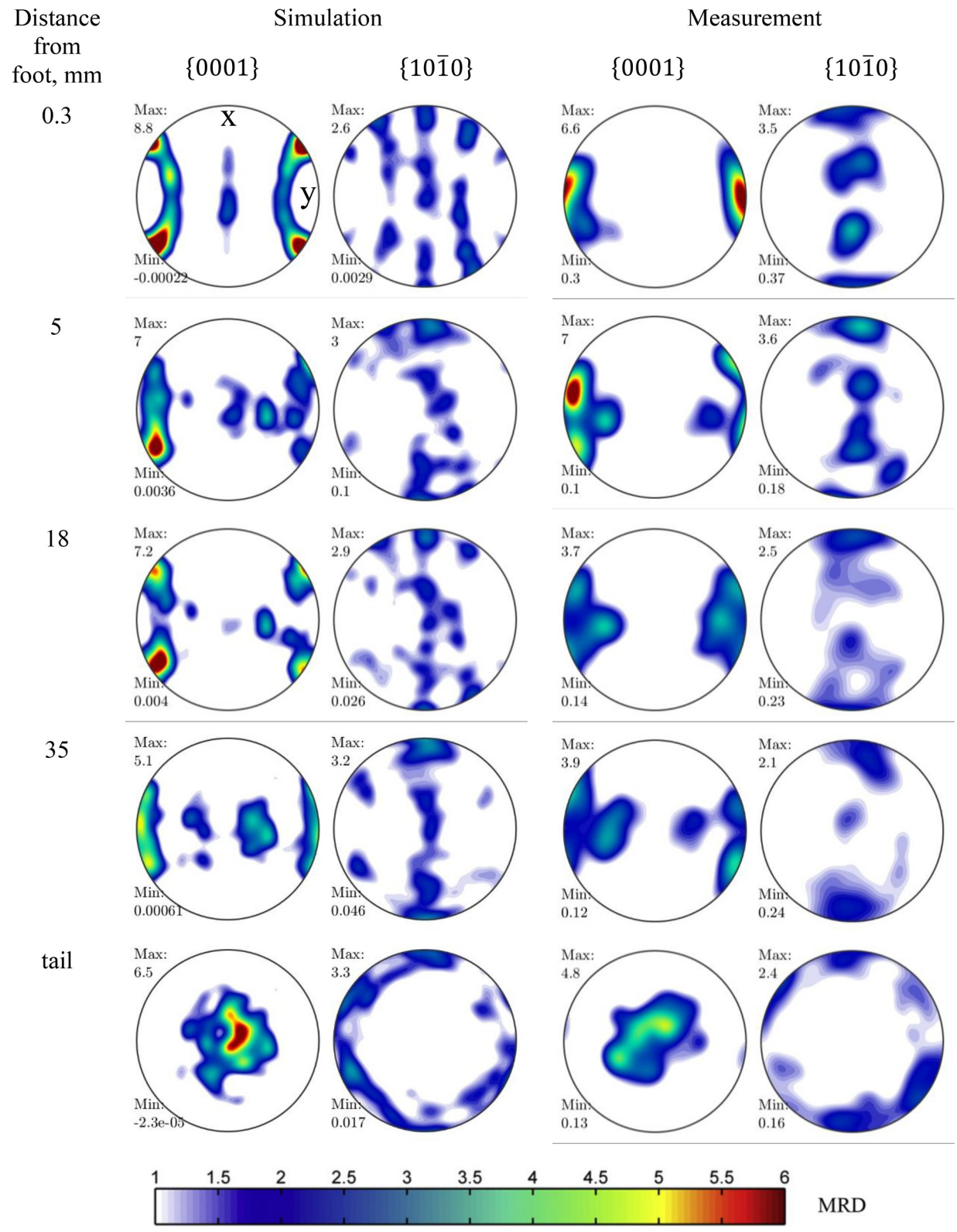

Fig. 14. Pole figures showing the comparison between measure (by EBSD) and predicted texture evolution after the 243 m/s impact as a function of the distance from the foot.

strain-rate sensitivity. The standalone VPSC model is first verified to reproduce the stress-strain response measured from quasi static to split Hopkinson pressure bar deformation conditions in simple compression. Subsequently, the FE-VPSC model is verified by simulating the spatial variation of deformation twinning under simple compression. Finally, the FE-VPSC model is used to simulate the dimensional changes and microstructure evolution in 4-point bending and Taylor impact cylinder tests. Comparisons with experiments show that the model successfully predicts both the deformed shapes of four beams under quasi-static 4-point bending deformation and the deformed shapes of three cylinders after their impact at speeds of 100 m/s, 170 m/s and 243 m/s. For the beams, the model further achieves good agreement between the calculated and experimental axial strains along the bending direction at the axial center of the beams. A good agreement is also achieved between the predicted and measured spatial variation in texture and twinning upon the impact for three cylinders. It is observed and predicted that slip and especially twinning form peak texture components aligning the crystallographic **c**-axes and the compression direction (cylinder axis). As the standalone VPSC model was primarily adjusted using a set of monotonic and split Hopkinson pressure bar experimental stress-strain curves, the FE-VPSC simulations in bending and impact can be largely regarded as predictions. Comparisons in terms of simulated and measured sample geometries, evolution of texture, and twin volume fractions after the impacts are used to slightly refine the model parameters to achieve good predictions across a broad range of strain rates. In summary, the FE-VPSC model captures with good accuracy the evolution of anisotropic material flow as a consequence of microstructural evolution and hard-to-deform crystallographic directions along with the development of gradients in texture and twinning through the geometries. Importantly, the impact predictions based on the dislocation density-based hardening law and underlying thermally activated glide suggest that the dislocation glide remains thermally activated at the strain-rates in the Taylor impact tests.

Declaration of Competing Interest

The authors declare that they have no known competing financial interests or personal relationships that could have appeared to influence the work reported in this paper.

Acknowledgements

This research was sponsored by the U.S. National Science Foundation and was accomplished under the CAREER grant no. CMMI-1650641.

Supplementary materials

Supplementary material associated with this article can be found, in the online version, at doi:10.1016/j.ijimpeng.2020.103655.

Appendix A

This appendix presents the main equations pertaining to the dislocation density-based hardening law used to evolve resistances to slip and twin modes. The slip system resistances evolve based on:

$$\tau_c^s = \tau_0^\alpha + \tau_{0,HP}^\alpha + \tau_{for}^s + \tau_{deb}^\alpha. \tag{A1}$$

The right hand side of Eq. (A1) consists of several terms. The initial value of slip resistances per mode is:

$$\tau_0^\alpha = A^\alpha\left(1 + B^\alpha \log\left(\frac{\dot{\varepsilon}}{\dot{\varepsilon}_{ref}}\right)\right)\exp\left(-\frac{T}{C^\alpha}\right)(1 + E^\alpha \text{lognormal}(\sigma^\alpha, \nu^\alpha)), \tag{A2}$$

where A^α, B^α, and C^α are fitting constants. The variables are temperature, T and strain-rate, $\dot{\varepsilon}$, which is an effective norm of the applied strain-rate i.e. $\dot{\varepsilon} = \sqrt{\frac{2}{3}}|\dot{\boldsymbol{\varepsilon}}|$. Furthermore, E^α is also a fitting constant with the lognormal terms, σ^α and ν^α, for capturing the saturation at high temperatures. The barrier contribution to the resistance is:

$$\tau_{0,HP}^\alpha = \mu^\alpha(T) HP^\alpha \sqrt{\frac{b^\alpha}{d_g}}, \tag{A3}$$

where b^α is the Burgers vector magnitude, d_g is the grain size evolving to a mean-free-path measure with twins present in the grain, $\mu^\alpha(T) = 40.06 - 0.022T$ [GPa] is the temperature dependent shear modulus, and HP^α is a Hall-Petch-like fitting parameter. The initial structure (Appendix B) consists of equiaxed grains with an average size of 25 μm. If a grain twins, the $\tau_{0,HP}^\alpha$ term becomes τ_{HP}^s, which is defined per system, s, as $\tau_{HP}^s = \frac{f^{pts} - f^{pts,0}}{f^{pts,max} - f^{pts,0}}\mu^\alpha(\mathrm{T}) HP^\alpha \sqrt{\frac{b^\alpha}{d_{mfp}^s}}$, where $d_{mfp}^s = \frac{(1 - f^{pts})d_c}{\sin(\alpha)}$ is a measure of mean free path for slip system s [59, 60]. Twin system which created the twin in the parent grain accommodated the most shear strain of all twin systems and is identified as the predominant-twin-system (PTS), α is the angle between the given slip plane and the PTS plane and, finally, $d_c = \frac{d_g}{n^{lamellas}}$ is the distance between twin lamellae. The distance is estimated as the ratio of the average grain size, d_g, and a nominal number of lamellae per grain, $n^{lamellas}$. The value of $n^{lamellas} = 5$ is used for Zr. The barrier factor, $\frac{f^{pts} - f^{pts,0}}{f^{pts,max} - f^{pts,0}}$, includes constants $f^{pts,\,0}$ and $f^{pts,\,max}$ representing the minimum, i.e. the nucleation volume fraction of 0.02, and the maximum volume

fraction that a PTS can take in a grain, respectively. The maximum volume fraction, $f^{pts,\ max}$, is calibrated to be 0.95 for primary twins and 0.1 for secondary twins. Upon nucleation, the growth of twins is accomplished by transferring the volume fraction from the parent grain to the twin as a result of shearing on the given twinning system, t, i.e. $\Delta f^t = \frac{\Delta\gamma^t}{S^\beta}$, where $\Delta\gamma^t$ is the shear increment, S^β is the characteristic shear, and Δf is the increment in volume fraction. The s dislocation densities in the twin are inherited from the parent grain. The forest ρ^s_{for} and debris ρ_{deb} terms evolve with corresponding dislocation populations using:

$$\tau^s_{for}(\dot{\varepsilon},\ T) = b^\alpha \mu^\alpha(T)\sqrt{\sum_{s'} \chi^{ss'} \rho^{s'}_{for}(\dot{\varepsilon},\ T)}, \tag{A4}$$

$$\tau^\alpha_{deb}(\dot{\varepsilon},\ T) = k_{deb}\mu^\alpha(T) b^\alpha \sqrt{\rho_{deb}(\dot{\varepsilon},\ T)} \log\left(\frac{1}{b^\alpha\sqrt{\rho_{deb}(\dot{\varepsilon},\ T)}}\right). \tag{A5}$$

The dislocation density evolves as a result of the competition between rate of dislocation generation and rate of dislocation removal due to dynamic recovery. Forest dislocation evolution is given by:

$$\frac{\partial \rho^s_{for}}{\partial \gamma^s} = \frac{\partial \rho^s_{gen,for}}{\partial \gamma^s} - \frac{\partial \rho^s_{rem,for}}{\partial \gamma^s} = k^s_1\sqrt{\rho^s_{for}} - k^s_2(\dot{\varepsilon},\ T)\rho^s_{for}. \tag{A6}$$

Certain fraction of removed forest dislocations is transformed into debris:

$$d\rho_{deb} = q^\alpha b^\alpha \sqrt{\rho_{deb}} \frac{\partial \rho^s_{rem,for}}{\partial \gamma^s} |d\gamma^s|. \tag{A7}$$

In these equations, k^s_1 is a fitting coefficient governing the rate of dislocation generation, while k^s_2 is temperature and rate sensitive dislocation removal coefficient calculated as:

$$k^s_2 = \frac{k^s_1}{\sqrt{\sum_{s'} (\chi^{-1})^{ss'} \left(\frac{\tau^{s'}_{sat}}{b^{\alpha'}\mu^{\alpha'}}\right)^2}},\ \tau^s_{sat} = \frac{D^\alpha (b^\alpha)^3 g^\alpha \mu^\alpha}{D^\alpha (b^\alpha)^3 - kT\log\left(\frac{\dot{\varepsilon}}{\dot{\varepsilon}_0}\right)}. \tag{A8}$$

In Eq. (A8), k is the Boltzmann constant, $\dot{\varepsilon}_0$ is a reference strain rate taken to be 10^9 /s, g^α is an activation energy, $\chi^{ss'}$ is a matrix consisting of dislocation interaction coefficients, and D^α is the drag stress. In order to minimize the number of fitting constants, only the diagonal terms of $\chi^{ss'}$ are set to typical values of 0.81 [72].

The twin resistance is:

$$\tau^t_c = \tau^\beta_0 + \tau^t_{0,HP} + \tau^\beta_{slip}. \tag{A9}$$

The right hand side of Eq. (A9) consists of an initial friction term τ^β_0 (independent on temperature and strain rate), a barrier term $\tau^t_{0,HP}$, and a term coupling the twin resistance and hardening due to slip. The first term is:

$$\tau^\beta_0 = \tau^\beta_{prop} + (\tau^\beta_{crit} - \tau^\beta_{prop})\exp\left(-\frac{\sum \rho^s_{for}}{n^\alpha \rho^s_{sat}}\right), \tag{A10}$$

with τ^β_{crit} andτ^β_{prop} are the critical nucleation and propagation stresses. The second and the third terms are:

$$\tau^t_{0,HP} = \frac{HP^\beta}{\sqrt{d_g}}, \tag{A11}$$

$$\tau^\beta_{slip} = \sum_s C^{\alpha\beta} b^\beta \mu^\alpha(T) b^\alpha \rho^s_{for}, \tag{A12}$$

where b^β is the Burgers vector magnitude and $C^{\beta\alpha}$ is the coupling matrix in function of strain-rate. In closing, we indicate that the twin reorientation due to secondary twinning is also modeled. To this end, secondary twins can nucleate when a primary twin fraction per grain reaches a volume fraction of 0.8. Upon nucleation of secondary twins, their propagation from the volume of primary twins is modeled in the same way as the primary twins from parent grains.

Appendix B

This appendix shows IPF maps in Fig. B1, Fig. B2, and Fig. B3 for the three cylinders after deformation.

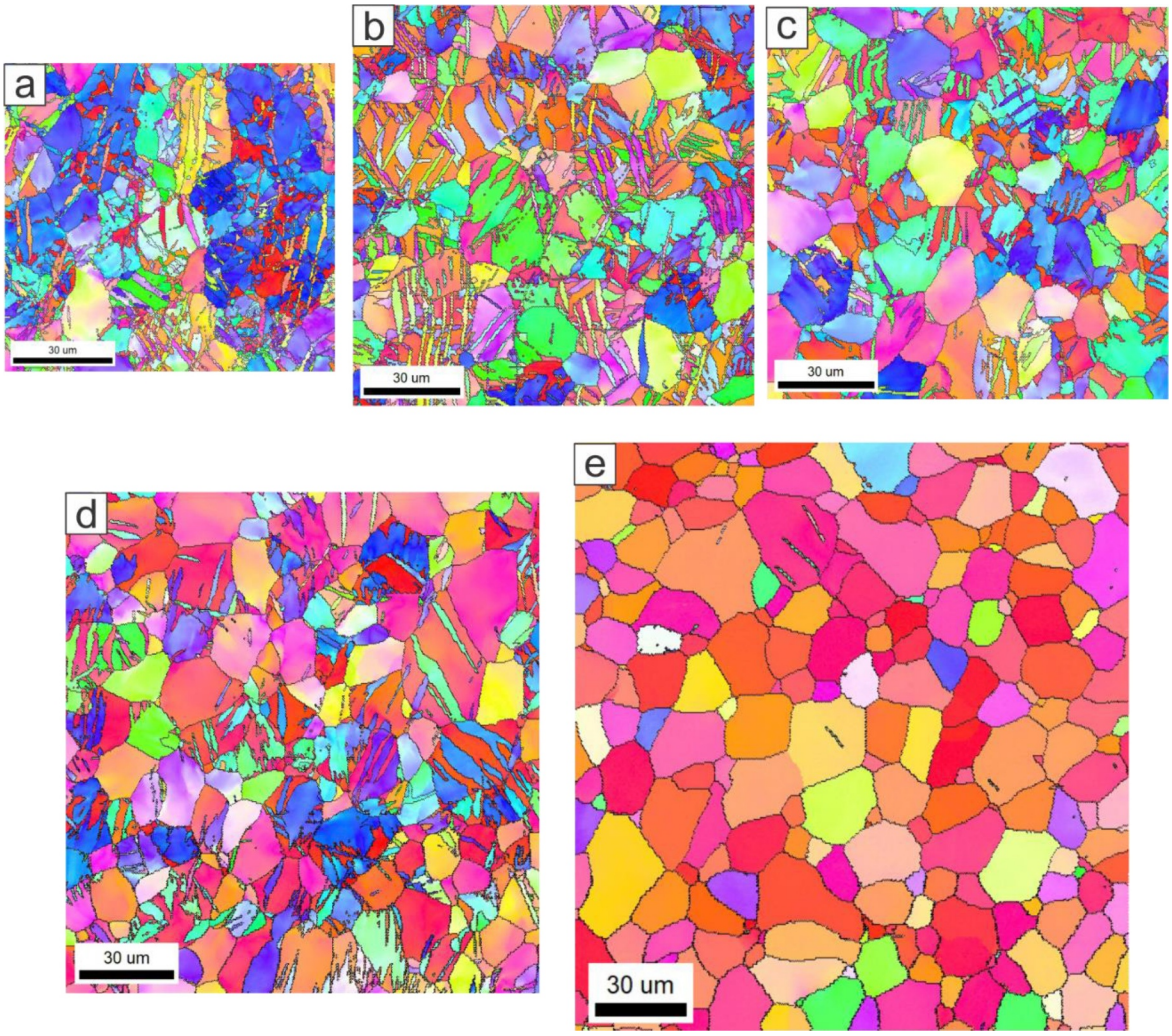

Fig. B1. Inverse pole figure (IPF) maps, measured at the following distances from the foot: (a) 0.1 mm, (b) 2 mm, (c) 8 mm, (d) 14 mm, (e) tail, showing microstructural evolution in the Zr cylinder after its impact carried out at 100 m/s. The colors in the maps depict the orientation of the z (TT) sample axis relative to the local lattice frame, according to the standard IPF triangle. The triangle and the sample axis are the same as in Fig. B2. The micron-bar in the maps is 30 μm.

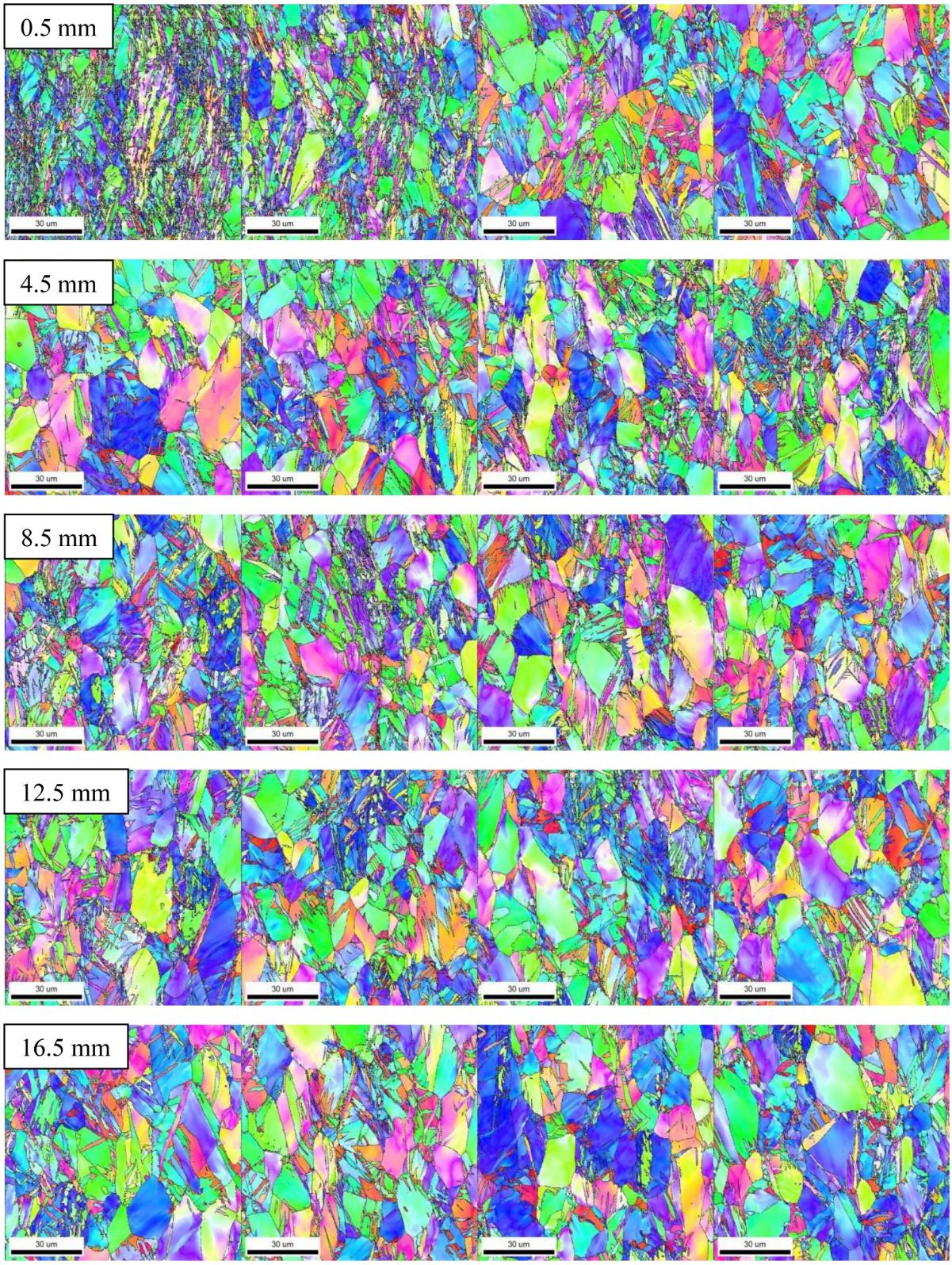

Fig. B2. Inverse pole figure (IPF) maps, measured along the axis of the cylinder with 1 mm spacing in between, showing microstructural evolution in the Zr cylinder after its impact carried out at 170 m/s. Numbers in the upper, left corner represents a distance from the foot. The colors in the maps depict the orientation of the z (TT) sample axis relative to the local lattice frame, according to the standard IPF triangle. The micron-bar in the maps is 30 μm.

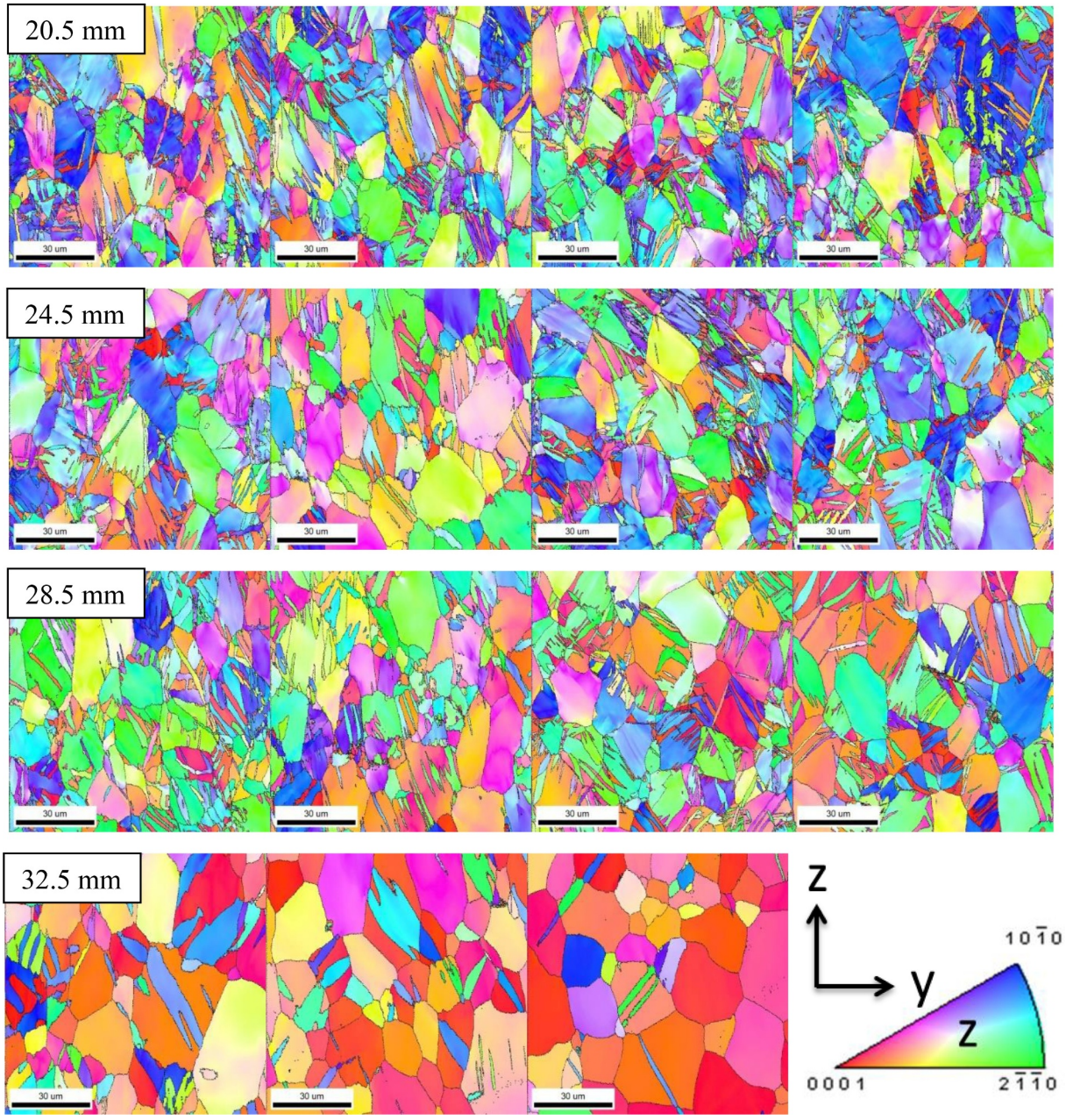

Fig. B2. (*continued*)

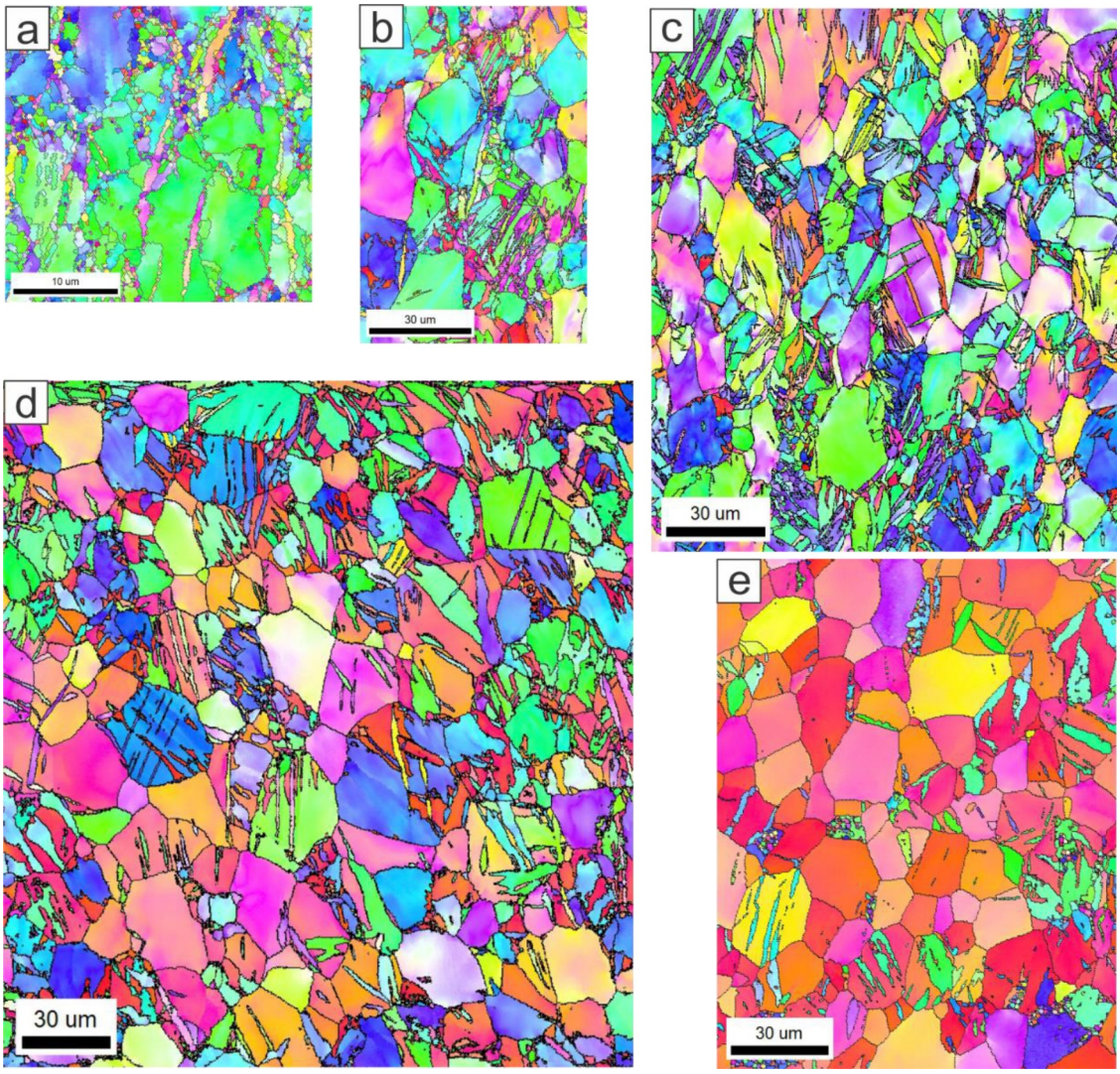

Fig. B3. Inverse pole figure (IPF) maps, measured at the following distances from the foot: (a) 0.3 mm, (b) 5 mm, (c) 18 mm, (d) 31 mm, (e) tail, showing microstructural evolution in the Zr cylinder after its impact carried out at 243 m/s. The colors in the maps depict the orientation of the z (TT) sample axis relative to the local lattice frame, according to the standard IPF triangle. The triangle and the sample axis are the same as in Fig. B2. The micron-bar in the maps is 30 μm.

References

[1] Nielsen R. Zirconium and Zirconium Compounds, in: Ullmann's Encyclopedia of Industrial Chemistry. KGaA. Wiley-VCH Verlag GmbH & Co; 2000.

[2] Lemaignan C, Motta AT. Zirconium Alloys in Nuclear Applications, in: Materials Science and Technology. KGaA. Wiley-VCH Verlag GmbH & Co; 2006.

[3] Capolungo L, Beyerlein IJ, Kaschner GC, Tomé CN. On the interaction between slip dislocations and twins in HCP Zr. Mater. Sci. Eng. A 2009;513-514:42–51.

[4] Chen SR, Kocks UF. High-Temperature Plasticity in Copper Polycrystals, High Temperature Constitutive Modeling - Theory and Application, in: A.D. Freed and K.P. Walker, eds., Atlanta, GA. Am. Soc. Mech. Eng. 1991:1–12.

[5] P.S. Follansbee, High Strain Rate Compression Testing - The Hopkinson Bar, in, 9th edn. Vol. 8, Am. Soc. Metals, Metals Park, Ohio, 1985, pp. 198-203.

[6] Knezevic M, McCabe RJ, Tomé CN, Lebensohn RA, Chen SR, Cady CM, Gray Iii GT, Mihaila B. Modeling mechanical response and texture evolution of α-uranium as a function of strain rate and temperature using polycrystal plasticity. Int. J. Plast. 2013;43:70–84.

[7] Knezevic M, Beyerlein IJ, Lovato ML, Tomé CN, Richards AW, McCabe RJ. A strain-rate and temperature dependent constitutive model for BCC metals incorporating non-Schmid effects: Application to tantalum–tungsten alloys. Int. J. Plast. 2014;62:93–104.

[8] Knezevic M, Carpenter JS, Lovato ML, McCabe RJ. Deformation behavior of the cobalt-based superalloy Haynes 25: experimental characterization and crystal plasticity modeling. Acta. Mater. 2014;63:162–8.

[9] Zecevic M, McCabe RJ, Knezevic M. Spectral database solutions to elasto-visco-plasticity within finite elements: application to a cobalt-based FCC superalloy. Int. J. Plast. 2015;70:151–65.

[10] Taylor GI. The use of flat-ended projectiles for determining dynamic yield stress. I. Theoretical considerations, in: Proceedings of the Royal Society of London A: Mathematical, Physical and Engineering Sciences. The Royal Society; 1948. p. 289–99.

[11] Maudlin P, Gray G, Cady C, Kaschner G. High–rate material modelling and validation using the Taylor cylinder impact test, Philosophical Transactions of the Royal Society of London A: Mathematical. Phys. Eng. Sci. 1999;357:1707–29.

[12] Lee E, Tupper S. Analysis of plastic deformation in a steel cylinder striking a rigid target. J. Appl. Mech 1954;21:63–70.

[13] Hawkyard J. A theory for the mushrooming of flat-ended projectiles impinging on a flat rigid anvil, using energy considerations. Int. J. Mech. Sci. 1969;11:313–33.

[14] Maudlin P, Bingert J, House J, Chen S. On the modeling of the Taylor cylinder impact test for orthotropic textured materials: experiments and simulations. Int. J. Plast. 1999;15:139–66.

[15] Plunkett B, Cazacu O, Lebensohn R, Barlat F. Elastic-viscoplastic anisotropic modeling of textured metals and validation using the Taylor cylinder impact test. Int. J. Plast. 2007;23:1001–21.

[16] Kothari M, Anand L. Elasto-viscoplastic constitutive equations for polycrystalline

metals: application to tantalum. J. Mech. Phys. Solids 1998;46:51–83.
[17] Bingert J, Mason T, Kaschner G, Gray III G, Maudlin P. Deformation twinning in polycrystalline Zr: Insights from electron backscattered diffraction characterization. Metall. Mater. Trans. A 2002;33:955–63.
[18] Zecevic M, Knezevic M. A new visco-plastic self-consistent formulation implicit in dislocation-based hardening within implicit finite elements: Application to high strain rate and impact deformation of tantalum. Comput. Methods Appl. Mech. Eng. 2018;341:888–916.
[19] Zecevic M, Beyerlein IJ, McCabe RJ, McWilliams BA, Knezevic M. Transitioning rate sensitivities across multiple length scales: Microstructure-property relationships in the Taylor cylinder impact test on zirconium. Int. J. Plast. 2016;84:138–59.
[20] Zecevic M, Knezevic M. Modeling of Sheet Metal Forming Based on Implicit Embedding of the Elasto-Plastic Self-Consistent Formulation in Shell Elements: Application to Cup Drawing of AA6022-T4. JOM 2017;69:922–9.
[21] Zecevic M, Knezevic M, Beyerlein IJ, McCabe RJ. Texture formation in orthorhombic alpha-uranium under simple compression and rolling to high strains. J. Nuclear Mater. 2016;473:143–56.
[22] Zecevic M, Knezevic M. An implicit formulation of the elasto-plastic self-consistent polycrystal plasticity model and its implementation in implicit finite elements. Mech. Mater. 2019;136:103065.
[23] Knezevic M, McCabe RJ, Lebensohn RA, Tomé CN, Liu C, Lovato ML, Mihaila B. Integration of self-consistent polycrystal plasticity with dislocation density based hardening laws within an implicit finite element framework: Application to low-symmetry metals. J. Mech. Phys. Solids 2013;61:2034–46.
[24] Knezevic M, Al-Harbi HF, Kalidindi SR. Crystal plasticity simulations using discrete Fourier transforms. Acta. Mater 2009;57:1777–84.
[25] Knezevic M, Beyerlein IJ. Multiscale modeling of microstructure-property relationships of polycrystalline metals during thermo-mechanical deformation. Adv. Eng. Mater. 2018;20:1700956.
[26] Knezevic M, Jahedi M, Korkolis YP, Beyerlein IJ. Material-based design of the extrusion of bimetallic tubes. Comput. Mater. Sci 2014;95:63–73.
[27] Revil-Baudard B, Cazacu O, Flater P, Kleiser G. Plastic deformation of high-purity α-titanium: model development and validation using the Taylor cylinder impact test. Mech. Mater. 2015;80:264–75. Part B.
[28] Kaschner GC, Bingert JF, Liu C, Lovato ML, Maudlin PJ, Stout MG, Tomé CN. Mechanical response of zirconium—II. experimental and finite element analysis of bent beams,. Acta. Mater. 2001;49:3097–108.
[29] Hutchinson JW. Bounds and self-consistent estimates for creep of polycrystalline materials. Proc. R. Soc. Lond. Series A, Math. Phys. Sci. 1976;348:101–26.
[30] Asaro RJ, Needleman A. Texture development and strain hardening in rate dependent polycrystals. Acta Metall. Mater. 1985;33:923–53.
[31] Lebensohn RA, Tomé CN. A self-consistent anisotropic approach for the simulation of plastic deformation and texture development of polycrystals: Application to zirconium alloys. Acta Metall. Mater. 1993;41:2611–24.
[32] Lebensohn RA, Tomé CN, Castaneda PP. Self-consistent modelling of the mechanical behaviour of viscoplastic polycrystals incorporating intragranular field fluctuations. Philos. Mag. 2007;87:4287–322.
[33] Follansbee P, Kocks U. A constitutive description of the deformation of copper based on the use of the mechanical threshold stress as an internal state variable. Acta Metall 1988;36:81–93.
[34] Al-Harbi HF, Knezevic M, Kalidindi SR. Spectral approaches for the fast computation of yield surfaces and first-order plastic property closures for polycrystalline materials with cubic-triclinic textures. CMC: Computers, Materials, & Continua 2010;15:153–72.
[35] Knezevic M, Kalidindi SR, Fullwood D. Computationally efficient database and spectral interpolation for fully plastic Taylor-type crystal plasticity calculations of face-centered cubic polycrystals. Int. J. Plast. 2008;24:1264–76.
[36] Kalidindi SR, Duvvuru HK, Knezevic M. Spectral calibration of crystal plasticity models. Acta. Mater. 2006;54:1795–804.
[37] Shaffer JB, Knezevic M, Kalidindi SR. Building texture evolution networks for deformation processing of polycrystalline fcc metals using spectral approaches: Applications to process design for targeted performance. Int. J. Plast. 2010;26:1183–94.
[38] Knezevic M, Kalidindi SR, Mishra RK. Delineation of first-order closures for plastic properties requiring explicit consideration of strain hardening and crystallographic texture evolution. Int. J. Plast. 2008;24:327–42.
[39] Knezevic M, Kalidindi SR. Fast computation of first-order elastic-plastic closures for polycrystalline cubic-orthorhombic microstructures. Comput. Mater. Sci. 2007;39:643–8.
[40] Knezevic M, Zecevic M, Beyerlein IJ, Lebensohn RA. A numerical procedure enabling accurate descriptions of strain rate-sensitive flow of polycrystals within crystal visco-plasticity theory. Comput. Methods Appl. Mech. Engineering 2016;308:468–82.
[41] Jahedi M, Paydar MH, Zheng S, Beyerlein IJ, Knezevic M. Texture evolution and enhanced grain refinement under high-pressure-double-torsion. Mater. Sci. Eng. A 2014;611:29–36.
[42] Hosford WF, Caddell RM. Metal forming: mechanics and metallurgy. New York, USA: Cambridge University Press; 2011.
[43] Smith DH, Bicknell J, Jorgensen L, Patterson BM, Cordes NL, Tsukrov I, Knezevic M. Microstructure and mechanical behavior of direct metal laser sintered Inconel alloy 718. Mater. Charact. 2016;113:1–9.
[44] Jahedi M, Knezevic M, Paydar M. High-pressure double torsion as a severe plastic deformation process: experimental procedure and finite element modeling. J. Mater. Eng. Perform. 2015;24:1471–82.
[45] Jahedi M, Paydar MH, Knezevic M. Enhanced microstructural homogeneity in metal-matrix composites developed under high-pressure-double-torsion. Mater. Charact. 2015;104:92–100.
[46] Bhattacharyya A, Knezevic M, Abouaf M. Characterization of crystallographic texture and intra-grain morphology in cross-rolled tantalum. Metall. Mater. Trans. A 2015;46:1085–96.
[47] Zecevic M, Roemer T, Knezevic M, Korkolis Y, Kinsey B. Residual ductility and microstructural evolution in continuous-bending-under-tension of AA-6022-T4. Materials 2016;9:130.
[48] Segurado J, Lebensohn RA, Llorca J, Tomé CN. Multiscale modeling of plasticity based on embedding the viscoplastic self-consistent formulation in implicit finite elements. Int. J. Plast. 2012;28:124–40.
[49] Knezevic M, Lebensohn RA, Cazacu O, Revil-Baudard B, Proust G, Vogel SC, Nixon ME. Modeling bending of α-titanium with embedded polycrystal plasticity in implicit finite elements. Mater. Sci. Eng. A 2013;564:116–26.
[50] Zecevic M, Knezevic M, Beyerlein IJ, McCabe RJ. Origin of texture development in orthorhombic uranium. Mater. Sci. Eng. A 2016;665:108–24.
[51] Knezevic M, Crapps J, Beyerlein IJ, Coughlin DR, Clarke KD, McCabe RJ. Anisotropic modeling of structural components using embedded crystal plasticity constructive laws within finite elements. Int. J. Mech. Sci. 2016;105:227–38.
[52] Asaro RJ, Rice JR. Strain localization in ductile single crystals, J. Mech. Phys. Solids 1977;25:309–38.
[53] Asaro RJ. Geometrical effects in the inhomogeneous deformation of ductile single crystals. Acta Metallurgica 1979;27:445–53.
[54] Hill R, Rice JR. Constitutive analysis of elastic-plastic crystals at arbitrary strain, J. Mech. Phys. Solids 1972;20:401–13.
[55] Peirce D, Asaro RJ, Needleman A. An analysis of nonuniform and localized deformation in ductile single crystals. Acta Metall 1982;30:1087–119.
[56] Hill. Generalized constitutive relations for incremental deformation of metal crystals by multislip. J. Mech. Phys.Solids 1966;14:95–102.
[57] Mercier S, Molinari A. Homogenization of elastic–viscoplastic heterogeneous materials: Self-consistent and Mori-Tanaka schemes. Int. J. Plast 2009;25:1024–48.
[58] ABAQUS Version 6. Dassault Systèmes. RI, USA: Providence; 2017.
[59] Beyerlein IJ, Tomé CN. A dislocation-based constitutive law for pure Zr including temperature effects. Int. J. Plast. 2008;24:867–95.
[60] Proust G, Tomé CN, Kaschner GC. Modeling texture, twinning and hardening evolution during deformation of hexagonal materials. Acta. Mater. 2007;55:2137–48.
[61] Knezevic M, Zecevic M, Beyerlein IJ, Bingert JF, McCabe RJ. Strain rate and temperature effects on the selection of primary and secondary slip and twinning systems in HCP Zr. Acta. Mater. 2015;88:55–73.
[62] Akhtar A. Schmid's law and prismatic slip of zirconium. Scripta Metallurgica 1975;9:859–61.
[63] Akhtar A. Compression of zirconium single crystals parallel to the c-axis. J. Nuclear Mater. 1973;47:79–86.
[64] Akhtar A. Basal slip in zirconium. Acta Metall 1973;21:1–11.
[65] Cheadle B, Ells C, Evans W. The development of texture in zirconium alloy tubes. Journal of Nuclear Materials 1967;23:199–208.
[66] Knezevic M, Zecevic M, Beyerlein IJ, Bingert JF, McCabe RJ. Strain rate and temperature effects on the selection of primary and secondary slip and twinning systems in HCP Zr. Acta Mater 2015;88:55–73.
[67] Christian JW, Mahajan S. Deformation twinning. Progress in materials science 1995;39:1–157.
[68] Morrow BM, McCabe RJ, Cerreta EK, Tomé CN. Variability in EBSD statistics for textured zirconium. Mater. Sci. Eng. A 2013;574:157–62.
[69] M.A. Meyers, K.K. Chawla, Mechanical Behavior of Materials., Prentice Hall, Upper Saddle River, New Jersey, 1998.
[70] Bhattacharyya JJ, Wang F, Wu PD, Whittington WR, El Kadiri H, Agnew SR. Demonstration of alloying, thermal activation, and latent hardening effects on quasi-static and dynamic polycrystal plasticity of Mg alloy, WE43-T5, plate. Int. J. Plast. 2016;81:123–51.
[71] Feather WG, Ghorbanpour S, Savage DJ, Ardeljan M, Jahedi M, McWilliams BA, Gupta N, Xiang C, Vogel SC, Knezevic M. Mechanical response, twinning, and texture evolution of WE43 magnesium-rare earth alloy as a function of strain rate: Experiments and multi-level crystal plasticity modeling. Int. J. Plast 2019;120:180–204.
[72] Kocks UF, Mecking H. Kinetics of Flow and Strain-Hardening. Acta Metall 1981;29:1865–75.